Construction and Building Materials 531 (2026) 146584

Contents lists available at ScienceDirect

Construction and Building Materials

journal homepage: www.elsevier.com/locate/conbuildmat

Mechanisms of long-term drying shrinkage in blended alkali-activated materials: The synergistic role of curing, microstructure, and gel chemistry

Mayank Gupta[1], Farnaz Aghabeyk[1], Christa Winterman, Guang Ye *

Department of Materials, Mechanics, Management & Design, Delft University of Technology, Delft, 2628 CN, The Netherlands

ARTICLE INFO

Keywords:
Drying shrinkage
Alkali-activated materials
Long-term data
Pore structure
Gel chemistry

ABSTRACT

The shrinkage behavior of alkali-activated materials (AAMs) is governed by the combined effects of precursor type, activator chemistry, and curing conditions, which control microstructure development and hydration gel formation. The synergistic interaction between these two factors ultimately dictates the material's shrinkage behavior. Due to the varying reaction kinetics of raw materials, short-term shrinkage measurements often fail to capture the long-term effects of these influencing factors on the material's dimensional stability. In this work, slag/fly ash-based AAM with varying alkali contents were cast and subjected to different durations of sealed curing before long-term drying shrinkage tests (up to one year). Pore structure and gel chemistry were analyzed to decouple their roles in shrinkage behavior. Results show that prolonged initial curing drastically reduces shrinkage, while early exposure to drying accelerates shrinkage kinetics. When exposed to drying at an early age, mixes with higher fly ash content exhibited the greatest shrinkage after one year, whereas if cured for a longer duration, mixes with higher slag content exhibited the highest shrinkage strain. Shrinkage–mass loss relationships followed a three-stage S-curve, reflecting the combined effects of pore structure and gel characteristics. By isolating specimens with comparable pore structures at the time of exposure, gel characteristics were shown to directly govern shrinkage, with higher Na/Si ratios disrupting the C-(N)-A-S-H gel network and increasing shrinkage. Thus, this work bridges microstructural insights with practical mix design, enabling the development of AAM binders with reduced shrinkage and improved durability.

1. Introduction

Alkali-activated materials (AAMs), which are primarily produced by mixing a high alkaline solution (such as sodium hydroxide or sodium silicate) with aluminosilicate precursors such as ground granulated blast furnace slag (GGBS) or fly ash (FA), have emerged as a promising alternative to the Portland cement (PC) [1–4]. AAMs offer a lower carbon footprint and often exhibit comparable or even superior properties to their PC counterparts. Despite their low carbon footprints, these materials are facing hindrance in the applications, particularly due to uncertainty with the volume stability (autogenous and drying shrinkage) [5,6]. When restrained due to reinforcement or external support, high eigen stresses are induced in concrete, which can cause cracking and lead to ingress of deleterious fluids, reducing the durability of the structures [7].

It has been reported in different literature that AAMs have higher shrinkage relative to their PC counterparts [8]. The understanding of the mechanisms of shrinkage in PC paste has been studied for a long time and is well understood. The effect of different parameters (such as water to binder (w/b) ratio, types of cement, chemical additives and gel characteristics, etc.) has been well reported in the literature [9]. In some cases, the shrinkage of the PC was found to be directly related to the mass loss of the specimens with time [10]. However, the mechanism of shrinkage in AAMs is more complex, particularly due to the complex microstructure development of the materials as a result of different mix design parameters such as w/b, amount of alkali, concentration of alkali, type and amount of aluminosilicate precursors, and curing conditions [10–13]. These parameters, along with physical and chemical characteristics of the precursors and activator, influence the microstructure development and gel chemical compositions [10,14–16]. The driving force for shrinkage in AAMs is capillary action, which depends on the paste's pore structure and relative humidity (RH). The Kelvin equation describes the relationship between the curvature of the liquid-vapor surface (the meniscus) and the RH as given below:

$$r_c = \frac{-2\gamma V_m}{RT \ln RH} \quad (1)$$

* Corresponding author.
E-mail address: G.Ye@tudelft.nl (G. Ye).
[1] Mayank Gupta and Farnaz Aghabeyk have contributed equally to this manuscript.

https://doi.org/10.1016/j.conbuildmat.2026.146584
Received 9 January 2026; Received in revised form 2 April 2026; Accepted 1 May 2026
Available online 13 May 2026

where γ is the surface tension, V_m is the molar volume of liquid, r_c is the meniscus radius, R is the gas constant, and T is the temperature. Lower pore size has a lower radius of the liquid-vapor meniscus. Further, the Young–Laplace equation provides the relationship between the capillary stress (σ_c) and the radius of the meniscus

$$\sigma_c = \frac{-2\gamma \cos\theta}{r_c} \quad (2)$$

Here θ refers to the contact angle denoting the hydrophilicity of the pore wall. As drying progresses and RH decreases, the radius of curvature of the meniscus reduces, leading to a significant increase in capillary stress. These stresses are transmitted to the solid skeleton, ultimately resulting in macroscopic shrinkage.

One of the main reasons for elevated shrinkage in AAMs is attributed to the finer pore size distribution of these materials, as reported by Collines and Sanjayan [17]. The pore size distribution of these materials is greatly influenced by the amount and type of precursor and activator [18]. In addition to the pore size distribution, gel characteristics also influence the shrinkage of AAMs. Ye and Radlińska have studied the shrinkage of alkali-activated slag (AAS) and concluded that higher shrinkage in AAS is likely due to the rearrangement and reorganization of calcium-alumina-silicate hydrate (C-A-S-H) gels [10]. As a result of this, different mitigation strategies will have different effects on the shrinkage mitigation [15,19–23].

The synthesis of alkali-activated binders blended with GGBS and FA has gained more attention, as both the precursors complement each other, providing a mix with adequate strength (curing at room temperature) and workability [14,24,25]. GGBS reacts faster with the alkali, resulting in rapid microstructure development, while FA has a slower reaction rate [26,27]. The pore structure of such blended materials is dependent on the GGBS/FA ratio of its constituents [28]. Due to such differences in the reaction rate, initial curing also becomes crucial and plays a role in the microstructure development and ultimately the shrinkage when exposed to drying conditions. Shen et al. conducted shrinkage measurements for alkali-activated GGBS and FA binders, which were cured for 2 days before being exposed to drying, and reported higher shrinkage in specimens with higher GGBS content [29]. Rashad reported analogous trends for specimens cured for 2 days before drying [30]. In contrast, Wang and Ma investigated drying shrinkage in AAMs with varying GGBS/FA ratios (0%, 30%, 50%, and 70% FA), following an initial 3-day curing period [31]. Their study indicated that the mix containing 30% GGBS exhibited the lowest shrinkage, a finding that diverges from the Shen et al. [29] and Rashad et al. [30]. This could be due to different initial curing durations. Most of the existing literature tends to only focus on the effect of the GGBS/FA ratio on drying shrinkage, keeping the initial curing time constant. Given the distinct reaction kinetics of GGBS and FA, the influence of initial curing on shrinkage is not uniform across different mix compositions. Hence, a more comprehensive investigation is essential to discern the combined influence of precursor composition and initial curing duration on drying shrinkage and microstructure in AAM systems.

Ye and Radlińska investigated the shrinkage behavior of AAS under different relative humidity (RH) conditions and found that shrinkage kinetics vary significantly between very low RH (< 30%) and moderate RH (50%–70%). At very low RH, shrinkage increases rapidly in the early stages and tends to stabilize over time. In contrast, at moderate RH levels, shrinkage progresses more gradually and does not reach a saturation even after 60 days of exposure [10]. Notably, most of the literature on shrinkage measurements of AAMs is limited to/up to 60–90 days of exposure to drying [10,19,29–31]. Ma and Ye [32] studied the long-term (180 days) shrinkage for alkali-activated FA and found that the specimens' shrinkage still did not reach saturation. Thus, such short-term measurements may not capture the long-term shrinkage behavior for the blended AAMs.

In addition to the microstructure characteristics, the intrinsic characteristics of the binding gels in AAMs, such as their composition, directly influence the drying shrinkage [10,14–16]. The composition of binding gels in AAMs is largely dictated by calcium availability in the system, which determines the predominant gel type [14,33]. In low-calcium systems, such as alkali-activated FA, a three-dimensional sodium aluminosilicate (N-A-S-H) gel typically forms [34]. Conversely, in high-calcium systems, such as AAS, calcium aluminosilicate hydrate (C-A-S-H) or alkali charge-balanced calcium aluminosilicate hydrate (C-(N)-A-S-H) gels typically dominate [35,36]. The formation of C-(N)-A-S-H gel has also been described as a hybrid gel phase when both C-A-S-H and N-A-S-H gels coexist, as seen in blended GGBS–FA binders [37,38]. Importantly, the structural properties of the binding gels in low-calcium and high-calcium systems differ significantly, which can affect drying shrinkage. For instance, N-A-S-H gel is believed to be more porous and less dense than C-A-S-H or C-(N)-A-S-H gels [39]. Moreover, differences in the compositional parameters of these binding gels, such as Ca/Si, Al/Si and Na/Si molar ratios, can further determine their nanostructure [40] and mechanical properties, such as their elastic modulus, which ultimately affects the drying shrinkage of the paste/concrete [41].

The available literature presents varied findings regarding the influence of compositional ratios on pore structure and, consequently, on shrinkage behavior. Mastali et al. have shown that increasing the Ca/Si ratio mitigates drying shrinkage by improving the gel's water-retaining properties and enhancing the pore structure [14]. Tao et al. and Xue et al. also studied the shrinkage behavior of alkali-activated binders and have also reported similar conclusions [37,42]. By contrast, Luo et al. found that partial replacement of GGBS with FA decreased Ca/Si and Na/Si ratios, enhanced pore refinement, and effectively reduced autogenous shrinkage [43]. Similar differences have been reported when discussing the influence of the Al/Si ratio on the pore structure and the resulting shrinkage behavior. In some studies, AAMs with a higher Al/Si ratio have demonstrated improved resistance to drying shrinkage [44,45] while in another study, the formation of N-A-S-H gel with a lower Al/Si ratio has been associated with a more compact gel structure, higher refinement of the pore structure, and finally, lower drying shrinkage [46]. Accordingly, the direct role of compositional parameters in shrinkage mechanisms remains unclear, largely because their effects are intertwined with pore structure. Such differences arise because most studies evaluate the shrinkage behavior under the simultaneous influence of multiple interdependent factors, including pore structure, mix design parameters, activator chemistry, water content, and gel formation [41,47–49]. Previous research has explored the relationship between gel formation and pore structure in AAMs, but a systematic investigation that isolates the specific influence of key gel characteristics (e.g., Ca/Si, Si/Al, or Na/Si ratios) is needed to highlight its influence on the drying shrinkage. As the pore structure primarily controls capillary stresses, while the gel composition and nanostructure influence the intrinsic deformation behavior of the solid matrix. However, these two factors are often interdependent, making it challenging to study the effect of one parameter while keeping the other constant/similar. Therefore, a systematic approach is required to specifically study the influence of only gel characteristics on the shrinkage of the AAMs; the pore structure should be kept the same (to isolate the effect of one from another). This can be achieved by maintaining a comparable pore structure while varying the gel chemistry, thereby enabling a more fundamental understanding of the governing mechanisms of shrinkage in AAMs.

To address the above-mentioned shortcomings in the current literature, this study undertakes a dedicated, long-term investigation of shrinkage in AAMs. The specific objectives of the current work are to (1) determine the combined influence of initial curing duration and precursor composition (GGBS/FA ratio) on the long-term (1 year) drying shrinkage behavior and microstructure of AAMs, extending well beyond the measurements typically reported; (2) analyze the long-term shrinkage kinetics of blended AAMs by correlating volume change

Table 1
Chemical composition of GGBFS and FA measured with XRF [wt.%].

Material	SiO_2	CaO	Al_2O_3	Fe_2O_3	Na_2O	K_2O	MgO	SO_3	P_2O_5	TiO_2	Others
GGBFS (%)	34.99	36.33	14.32	0.40	0.24	0.46	9.42	1.36	0.01	1.21	1.26
FA (%)	55.29	4.43	25.03	6.94	0.91	1.66	1.41	0.73	1.01	1.23	1.36

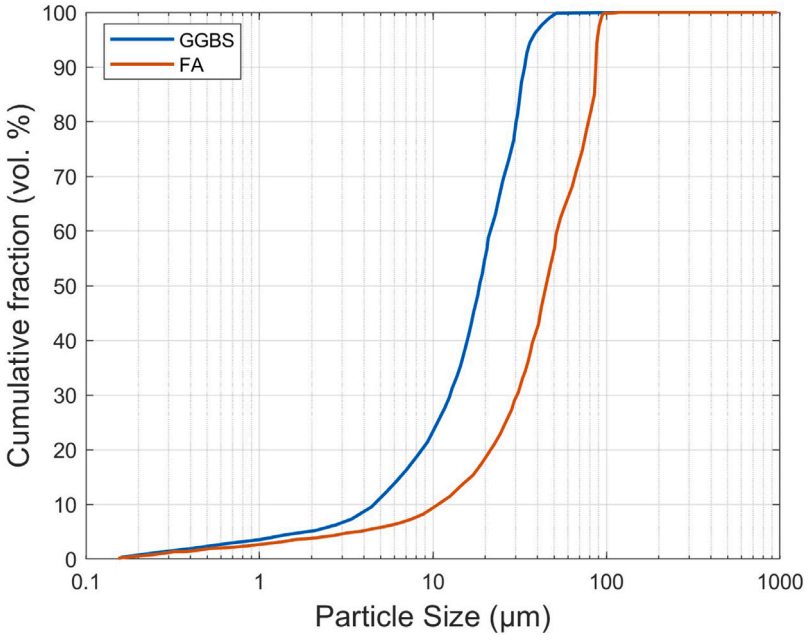

Fig. 1. Particle size distribution of the precursors in this study.

with mass loss over an extended drying period, providing a more complete understanding of their long-term stability; and (3) systematically isolate, for the first time, the influence of binding gel characteristics on drying shrinkage, independent of the influence of pore structure. Collectively, these objectives represent a significant step toward resolving the contradictions and measurement limitations that persist in the current literature.

To address the above objectives, this article is outlined as follows: details of the materials and experiments are provided in Section 2; subsequently, the experimental results are outlined in Section 3. Further, the detailed discussion of the experimental results is provided in Section 4, and finally, the conclusion is given in Section 5.

2. Materials and experimental methods

2.1. Materials and mix proportions

Two precursors used in the current study were GGBS and FA. GGBS was obtained from Ecocem Benelux B.V., while FA was obtained from Vliegasunie B.V. The chemical composition of GGBS and FA measured from X-ray fluorescence (XRF) is given in Table 1. Moreover, the mineralogical composition and particle size distribution (PSD) of GGBS and FA were reported in a prior study [50]. The PSDs, obtained by laser diffraction (Malvern Mastersizer), are presented in Fig. 1, with median particle sizes (D50) of 18.3 μm and 44.2 μm for GGBS and FA, respectively.

The alkaline activator used in this study was prepared by mixing water glass solution and sodium hydroxide. The water glass solution used in this study contains 15% Na_2O, 30% SiO_2, and 55% H_2O by weight. The activator was prepared by mixing the water glass solution and sodium hydroxide for 5-6 h to obtain a certain activator modulus (molar ratio of SiO_2/Na_2O). Subsequently, the activator was kept in the laboratory for 24 h before use. A water-to-precursor ratio (w/p) of 0.4 and an activator modulus of 1.0 was used for all the specimens. Five different mixes were prepared in this study, varying the proportion of GGBS (weight % GGBS in total weight of precursor) and alkali content (% weight Na_2O with respect to total precursor). Table 2 outlines all the mixes used in this study.

Table 2
Mix proportions of all mixes used in this study.

Mixes	GGBFS (wt.% in precursor)	FA (wt.% in precursor)	Na_2O (wt.% with total precursor)
S100N4	100	–	4
S70N4	70	30	4
S50N4	50	50	4
S70N5	70	30	5
S50N5	50	50	5

The mix design parameters were selected to reflect the most commonly utilized parameters in AAM research [51,52]. The two selected alkali contents and the range of GGBS/FA ratios increase the likelihood of obtaining mixes with a similar pore-size distribution and allow study of the effect of alkali content on the shrinkage behavior of AAMs. For the mixing process, firstly, GGBS and FA were dry-mixed in a Hobart paddle mixer for 120 s at 140 rpm. Further, the alkaline solution was added, and initial mixing was performed for 60 s at 140 rpm. After scraping the paste from the sides, the final mixing was performed for 60 s at 285 rpm. After the mixing procedure, the paste was used for different experimental methods, as explained in the next sections.

2.2. Experimental methods

2.2.1. Mechanical properties

Prism specimens with dimensions of 4 × 4 × 16 cm were used for the measurement of the mechanical properties, which include flexural and compressive strength. Mechanical properties were measured after 3, 7, 14, and 28 days of curing, with three specimens prepared for each

curing time. The specimens were cured under sealed curing conditions at 20 ± 1 °C. A three-point bending test was performed for all the specimens according to NEN-EN 196-1. Following the flexure strength measurement, the resulting halves of the prisms were subjected to a compressive strength test, following NEN-EN 196-1.

2.2.2. Drying shrinkage and weight loss

The drying shrinkage measurements were conducted following NEN-EN 12390-16. For the shrinkage and weight loss measurements, prism specimens with dimensions of 4 × 4 × 16 cm were prepared in accordance with NEN 196-1. After demoulding, the specimens were sealed by wrapping them in plastic foil to prevent moisture loss and stored at 20 ± 1 °C for different curing durations (3, 7, 14, and 28 days). Further, the specimens were exposed to a controlled drying environment with a temperature of 20 ± 1 °C and 55% RH. Three specimens were measured for each sample. The initial length (L_0) and weight (m_0) were measured by the digital length comparator with an accuracy of 0.001 mm and a balance with 0.1 g accuracy, respectively. The drying shrinkage strain (ϵ_t) at any time (t) is calculated according to Eq. (3), and the weight loss (w_t) using Eq. (4).

$$\epsilon_t = \frac{(L_0 - L_t)}{L_0} \tag{3}$$

Here L_t denotes the length of the specimen at time t.

$$w_t = \frac{(m_0 - m_t)}{m_0} * 100\% \tag{4}$$

Here m_t represents the weight of the specimen at time t. The shrinkage strain and mass loss were measured at regular time intervals for 1 year.

2.2.3. Porosity and pore size distribution

The porosity and pore size distribution of the different alkali-activated pastes were measured using Mercury intrusion porosimetry (MIP). After the mixing, the paste samples were kept in cylinders with a 25 mm diameter and 40 mm height and sealed using paraffin foil and the lid. Samples were kept in an environmental chamber with a temperature of 20 ± 1 °C for different curing times (3, 7, and 14 days). After these curing times, the samples were removed from the moulds and broken into small pieces of size 3–8 mm. The solvent exchange method was followed for hydration stoppage. The broken particles were immersed in isopropanol for 7 days, with isopropanol being refreshed once after the first 24 h. After 7 days, the samples were placed in a vacuum freeze-dryer for 21 days to ensure the removal of free water from the paste. One specimen was measured for each mix at each curing time. During the intrusion process, the equilibrium pressure (P) is related to the diameter (d) using the Washburn equation as given below:

$$d = \frac{4\gamma \cos\theta}{P} \tag{5}$$

where γ and θ represents the surface tension of mercury ($\gamma = 0.485$ N/m) and the contact angle ($\theta = 141°$), respectively. The maximum intrusion pressure was 210 MPa. It should be noted that the pore structure characterization was performed on sealed-cured specimens prior to drying exposure. This ensures that the measured pore structure reflects the intrinsic microstructure developed under identical curing conditions. The pore structure is expected to evolve during drying due to moisture loss and associated microstructural changes. The present measurements aim to capture the initial state of the material before the onset of drying shrinkage. This provides a common basis for evaluating the influence of mix design parameters and for identifying mixtures with comparable pore structures, which is essential for isolating the effect of gel characteristics on shrinkage behavior.

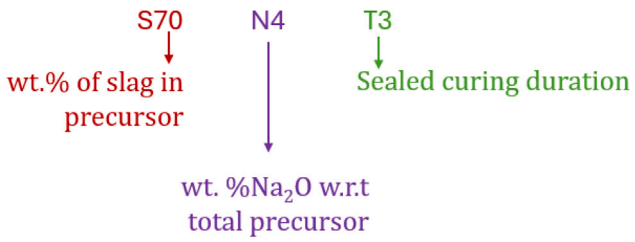

Fig. 2. Nomenclature of different specimens used in this study.

2.2.4. SEM analysis

The samples after the hydration stoppage were used for the SEM analysis. These were further impregnated with low-viscosity epoxy resin and then polished down to 0.25 μm. Further, the polished samples were analyzed using a FEI Quanta FEG 650 with back-scattering electron (BSE) mode at an acceleration voltage of 15 kV under low vacuum mode, with water vapor pressure kept at 1.0 Torr. A magnification of 1000x and a working distance of 10 mm were used for the images. Multiple images were taken for each sample, and the obtained SEM-BSE images were then used for image analysis using the Ilastik toolkit by applying the pixel classification workflow [53]. Different phases in the images were segmented based on their grayscale value. The chemical composition of the gel phase was investigated using the Energy Dispersive X-ray spectroscopy (EDX) detector integrated with the SEM. EDX point analysis was performed on selected samples, specifically targeting the gel phases. The point analysis was conducted at a magnification of 5000, maintaining an equal accelerating voltage and working distance.

3. Experimental results

This section discusses the experimental results in three subsections: first, the mechanical properties of different mixes are elaborated, second, the shrinkage and mass loss of different mixes are outlined, and finally, the porosity and pore size distribution of different mixes are described. Since different mix designs were used and experimental methods were performed at different stages of curing time, the following nomenclature is used in this study (Fig. 2).

3.1. Mechanical properties

Fig. 3 shows the development of compressive and flexural strength in mixtures with varying Na_2O contents over curing periods of 3, 7, 14, and 28 days. According to the results, both compressive and flexural strength are highly influenced by the composition of the precursor and the Na_2O content in the activator. Among the mixtures, S70N5 achieved the highest compressive strength, reaching 66.47 MPa at 28 days, while S100N4 showed the highest flexural strength at 28 days, measuring 12.94 MPa. As illustrated in Fig. 3, while a higher Na_2O content (5%) enhances compressive strength, it has an adverse effect on flexural strength, consistent with findings from previous studies [54]. The positive influence of higher Na_2O content on the compressive strength of mixtures is due to the enhanced geopolymerization reaction, as the higher concentration of OH^- ions from the activator accelerates the dissolution of Si^{4+} and Al^{3+} from precursors [54,55]. Conversely, the negative influence of high Na_2O content is likely due to the potential formation of micro-cracks, which create weakness zones that lower the flexural strength. Additionally, with an increase in the GGBS content, an enhancement in the strength development can be seen. This trend is likely due to the denser microstructure of GGBS-rich mixtures, which enhances the mechanical properties.

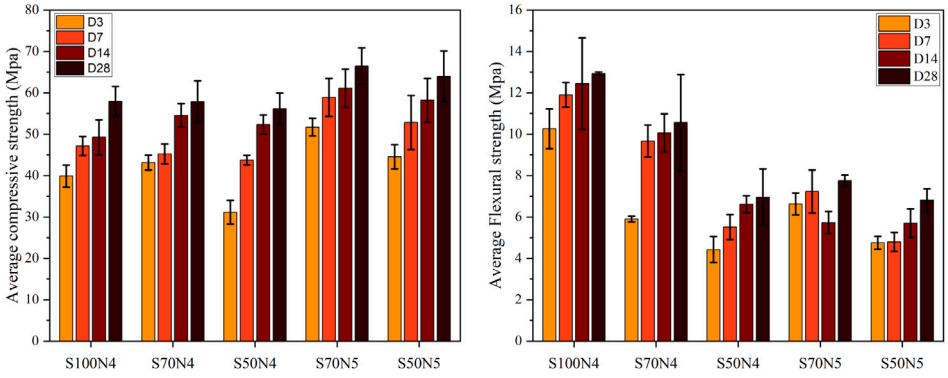

Fig. 3. Mechanical properties of alkali-activated pastes: (a) compressive strength and (b) Flexural strength.

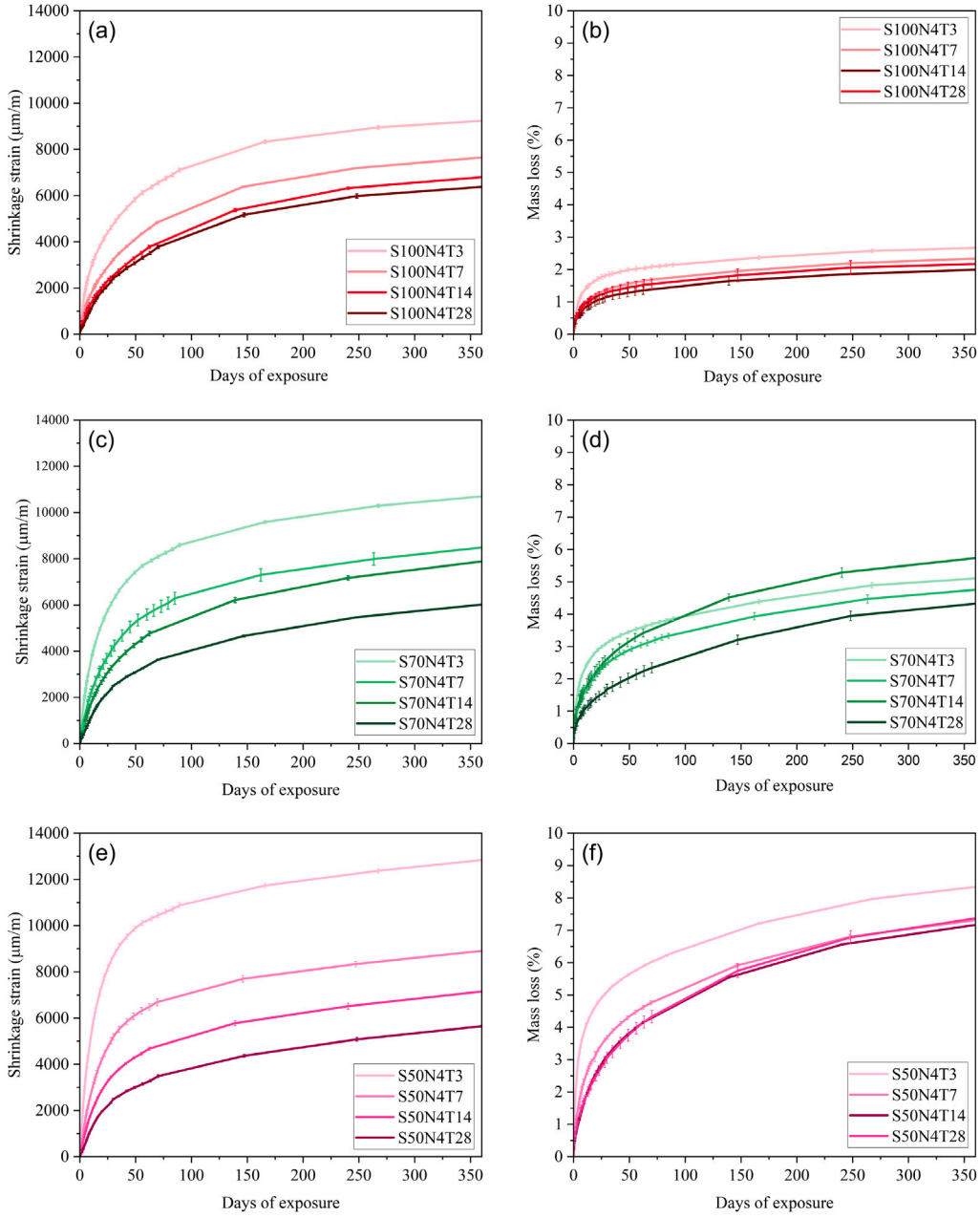

Fig. 4. Shrinkage strain and mass loss for different mixes with 4% alkali content.

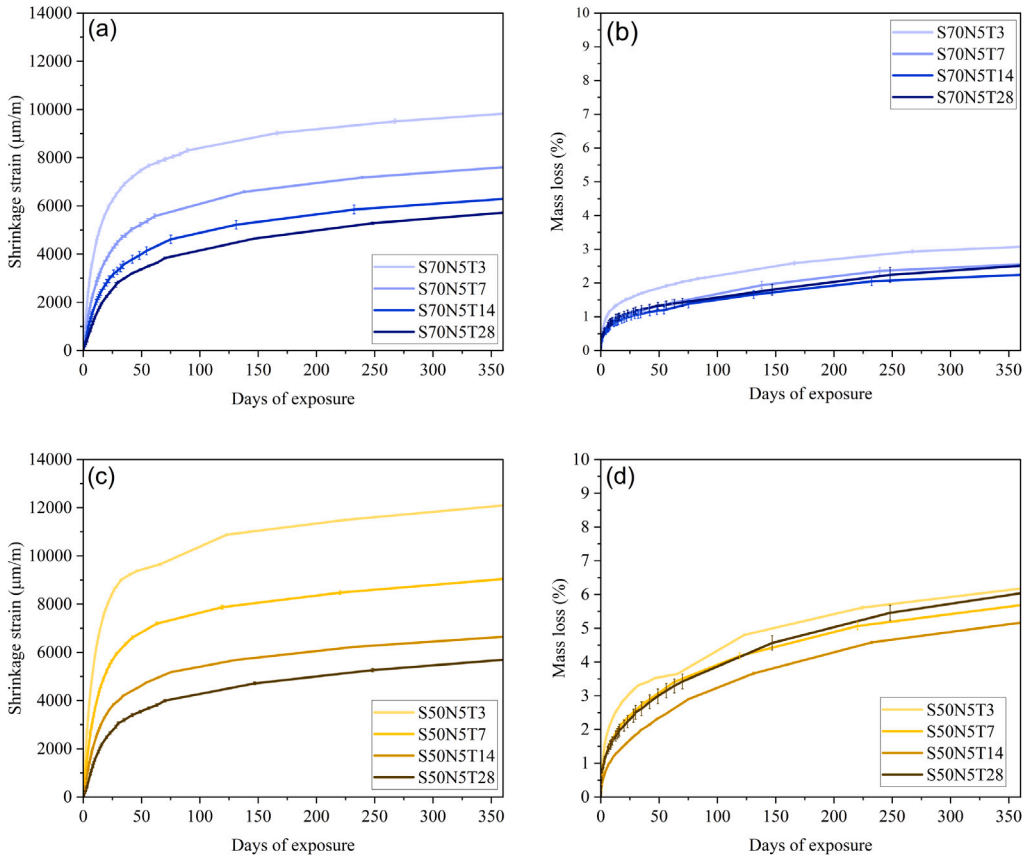

Fig. 5. Shrinkage strain and mass loss for different mixes with 5% alkali content.

3.2. Shrinkage and mass loss

Figs. 4 and 5 plot experimental data for the shrinkage and mass loss for mixes with 4% and 5% alkali content, respectively, which are exposed to drying after different initial sealed curing durations. It is important to note that the abscissa in all the plots in Figs. 4 and 5 refers to the time of exposure to drying environments. It is quite evident from all the plots in Figs. 4 and 5 that shrinkage strains decreased drastically when specimens were exposed to lower humidity environments after longer initial curing durations. With longer curing time, the microstructure of the pastes has become denser (with higher hydration), which provides higher resistance against the capillary stresses [56,57]. A similar trend can also be observed for the mass loss of different specimens, as plots reflect higher mass loss for specimens exposed to drying at early ages.

From Fig. 4(a), (c), and (e), it is apparent that, for the samples exposed to drying conditions early (for example, T3), the shrinkage strains were higher for the mix with higher FA content. The highest shrinkage strain was observed for the S50N4T3 specimen, which reached approximately 12500 μm/m after 1 year of exposure, while S100N4T3 observed a shrinkage strain of approximately 8500 μm/m. However, for the sample cured for a longer time (28 days), the shrinkage strain in mixes with different FA content was much closer to each other. The mix with 50% FA cured for 28 days (S50N4T28) observed the least shrinkage strain (approximately 5500 μm/m) after 1 year of exposure. Comparing Fig. 4(b), (d), and (f), it can be observed that higher mass loss is observed for specimens with higher FA content for a similar curing time. As the hydration of GGBS proceeds faster relative to FA, more water is bound in the formation of reaction products, which results in lower mass loss for the mix with higher GGBS content [26,27]. Additionally, the mixes with higher GGFS content have a dense microstructure, which also makes it difficult for water to evaporate (as can be seen in the porosity and pore size distribution data in Section 3.3). The denser microstructure for mixes with higher GGBS content provides higher resistance to shrinkage stresses. Fig. 4(c), (e) and Fig. 5(a), (c) plots shrinkage strains for mixes with two different alkali contents, i.e., 4 and 5% respectively. A reduction in the shrinkage strains has been observed with an increase in the alkali content for a similar ratio of GGBS and FA. For specimens cured for 28 days, the shrinkage strain decreased from 10500 μm/m to 9500 μm/m and 12500 μm/m to 11500 μm/m for S70 and S50, respectively, when the alkali content was increased from 4 to 5%. A similar trend of decrease in the mass loss of the specimens with increase in the alkali content is also reflected by comparing Fig. 4(d), (f) and Fig. 5(b), (d).

3.3. Porosity and pore size distribution

This section provides the MIP results (pore size distribution and cumulative pore volume) of alkali-activated pastes with varying GGBS and Na_2O contents at different curing ages. For the S50N5 mixture, only one curing time at 3 days (S50N5T3) was analyzed for further selection and comparison based on the pore size distribution. While this limits direct comparisons over time, the data provide insights into the initial pore structure and cumulative intrusion, serving as a baseline for understanding the effect of curing time in other mixtures.

3.3.1. Influence of curing time

The MIP results demonstrate that curing time significantly influences the pore structure and porosity of alkali-activated pastes. Across all samples (Fig. 5(a–h)), an increase in the curing time leads to a noticeable refinement of the pore structure and a reduction in porosity, indicating progressive densification of the matrix. For the S100N4 paste, cumulative intrusion decreases by approximately 46% from 3 to 28 days, accompanied by a shift toward finer pores. Similar trends are

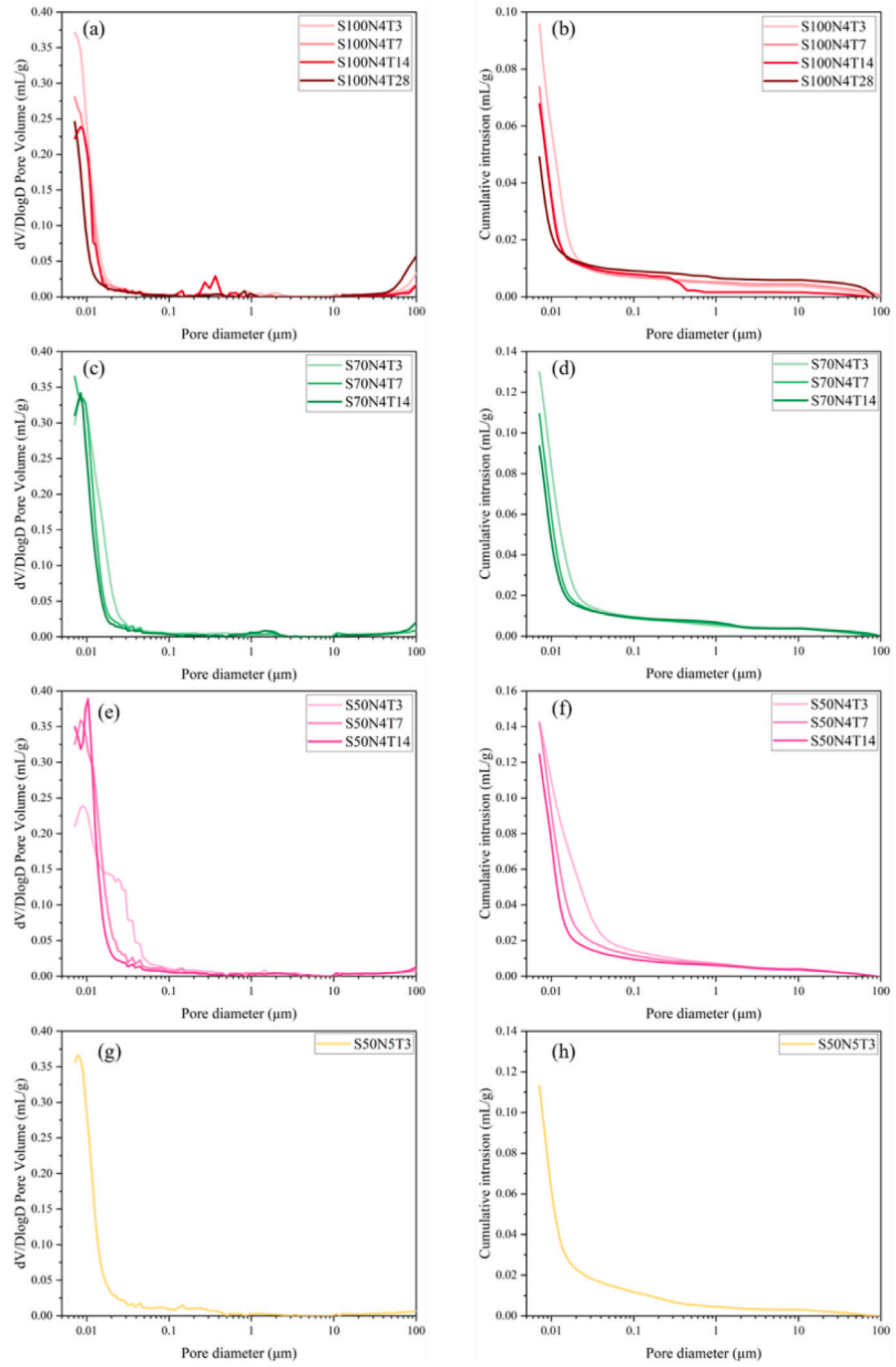

Fig. 6. Pore size distribution of alkali-activated pastes at different curing ages.

observed for the S70N4 mixture, where cumulative intrusion reduces by about 15% from 3 to 7 days and by 50% after 14 days of curing. In the S50N4 paste, curing time contributes to the disappearance of the pores in the 0.02–0.05 μm range and a 15% reduction in the total intrusion from 3 to 14 days of curing. Moreover, a comparison between S50N4 and S50N5 at the same curing time (3 days) reveals the influence of sodium oxide concentration on the pore structure. Despite having a higher sodium content (5 wt% Na_2O), the cumulative pore intrusion in S50N5 is lower than in S50N4, indicating reduced porosity. This suggests that a higher concentration of Na_2O the activator, promotes more extensive gel formation and matrix densification even at early curing stages.

3.3.2. *Influence of GGBS-to-FA ratio*

The critical role of the GGBS-to-FA ratio in controlling the pore structure and porosity of alkali-activated pastes is evident in Fig. 5. Increasing GGBS content leads to a refined pore structure and a decrease in the total porosity. For instance, in the S100N4 mixture, the cumulative pore intrusion is significantly lower compared to pastes with higher FA content, indicating a denser and more compact matrix for GGBS-rich alkali-activated pastes. In contrast, mixtures with lower GGBS content (e.g., S70N4 and S50N4) exhibit distinct peaks in the 0.002 μm range, suggesting the dominance of medium-sized capillary pores. Additionally, cumulative pore intrusion increases substantially with decreasing GGBS content, reflecting higher porosity. The S50N4 mixture shows a 77% increase in cumulative intrusion compared to S100N4, emphasizing the more porous nature of FA-rich

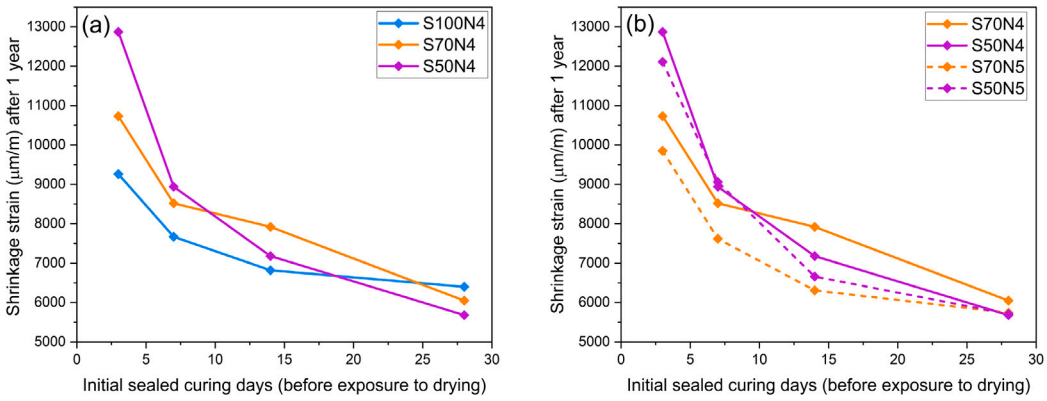

Fig. 7. Shrinkage strain of different mixes after one year of exposure with different initial sealed curing durations.

pastes. Interestingly, the pore structure of S50N4 also reveals a peak around 0.0015 μm, indicating the presence of smaller pores alongside capillaries.

4. Discussion

4.1. Drying shrinkage: curing, kinetics and mass loss dynamics

4.1.1. Effect of curing

Fig. 7(a) plots the shrinkage of mixes with different GGBS/FA ratios after one year of exposure to drying conditions after different initial sealed curing days. It can be observed that when samples are exposed to drying conditions after 3 days of curing, S50N4 samples showed the highest shrinkage strain, while S100N4 showed the lowest shrinkage strain. Since FA tends to react slowly relative to GGBS, the specimens with higher FA content have slower microstructure development. As a result, when samples are exposed to drying conditions at early ages, the specimens with higher FA content show higher shrinkage, as it has lower resistance to capillary stresses. When specimens were exposed to drying conditions after 28 days of curing, the differences in the shrinkage strain were reduced with different GGBS/FA ratios. However, the order of shrinkage strain is reversed, as S100N4 specimens showed the highest shrinkage strain, while S50N4 specimens showed the lowest shrinkage. The samples with higher GGBS content have a refined pore structure, resulting in higher capillary stresses and higher shrinkage. For intermediate curing durations between 3 and 28 days, a clear transition in shrinkage behavior is observed, indicating a shift in trends. The observed reversal in shrinkage ranking with curing duration can be explained by the competition between two governing mechanisms: (i) microstructural resistance, which refers to the stiffness and connectivity of the solid skeleton, which governs the ability of the material to resist capillary stresses and (ii) capillary stress development, which is primarily controlled by pore size refinement. At early ages, the microstructure is relatively weak and poorly connected, particularly in FA-rich systems, resulting in low stiffness and limited resistance to capillary stresses. Consequently, shrinkage is primarily governed by microstructural resistance, leading to higher shrinkage in mixes with higher FA content. This is also evident in the cumulative porosity and pore-size distribution data shown in Fig. 6(e) and (f), as S50N4T3 shows the highest porosity (among all specimens) and some pores in the range 0.02-0.06 μm. At later ages (after 28 days of curing), the microstructure becomes significantly denser, specifically for slag-rich systems, resulting in finer pores. This increases capillary stresses (as governed by the Kelvin equation), which then becomes the dominant mechanism controlling shrinkage. As a result, slag-rich mixes exhibit higher shrinkage despite having a denser matrix. This trend is consistent with the pore size distribution results shown in Fig. 6(a), where a higher proportion of finer pores is observed.

Fig. 7(b) illustrates the shrinkage strain of mixes with varying alkali contents after one year, with different durations of initial curing before exposure to drying conditions. It is evident that specimens with higher alkali content consistently exhibit lower shrinkage strains, irrespective of the initial curing duration. This reduction in shrinkage is particularly pronounced in mixes with higher GGBS content, highlighting the influence of alkali content on shrinkage behavior. Increased alkali content accelerates the geopolymerization process, resulting in higher hydration products. This densification due to higher reaction products reduces the susceptibility to shrinkage strains, especially in systems rich in GGBS, where the reaction kinetics are more responsive to higher alkali concentrations.

4.1.2. Shrinkage kinetics

This section compares the development of shrinkage strains of the different mixes, focusing on the effect of GGBS/FA ratio, alkali content, and curing time. In order to compare the shrinkage of different specimens, normalized strains (ϵ_n) are calculated using the equation given below:

$$\epsilon_n = \frac{\epsilon_t}{\epsilon_{365}} \tag{6}$$

Here ϵ_t and ϵ_{365} denote the shrinkage strain after t and 365 days of exposure, respectively. Fig. 8(a), (b), and (c) plot the normalized shrinkage strain for S100N4, S50N4, and S50N5, respectively. Horizontal black lines in Fig. 8 mark the normalized shrinkage strains of the specimens that are cured for 3 and 28 days (lowest and highest sealed curing duration in the current study) after 60 days of drying exposure. In all the subplots of Fig. 8, it is apparent that the normalized shrinkage strain after 60 days is higher for 3 days of initial sealed curing compared to 28 days of initial sealed curing. This observation indicates that exposure to drying conditions at early stages of hydration leads to a more rapid increase in shrinkage strain compared to samples cured for longer durations. Furthermore, for the 28-day curing period, the shrinkage has only reached 53%–66% for the shrinkage at 365 days, which shows that a substantial amount of shrinkage continues to occur at later stages of exposure (even beyond 60 days). This highlights the necessity for extended shrinkage measurement durations to fully capture the material's long-term behavior. The effect of initial curing conditions on shrinkage kinetics is more pronounced on mixes with higher FA content when the alkali content is kept constant. The ϵ_n for S100N4 changed from 0.67 to 0.53 (for 3 and 28 days of curing, respectively), while for S50N4 it changed significantly from 0.79 to 0.57 (for 3 and 28 days of curing, respectively). This is primarily due to the slower reaction and microstructure development of AAMs with higher FA. Due to the rapid hydration of S100N4, the microstructure has already evolved by up to 3 days, and a lower hydration rate occurs afterwards, compared to S50N4, where significant hydration occurs over the span of 3 to 28 days. This is also reflected in the

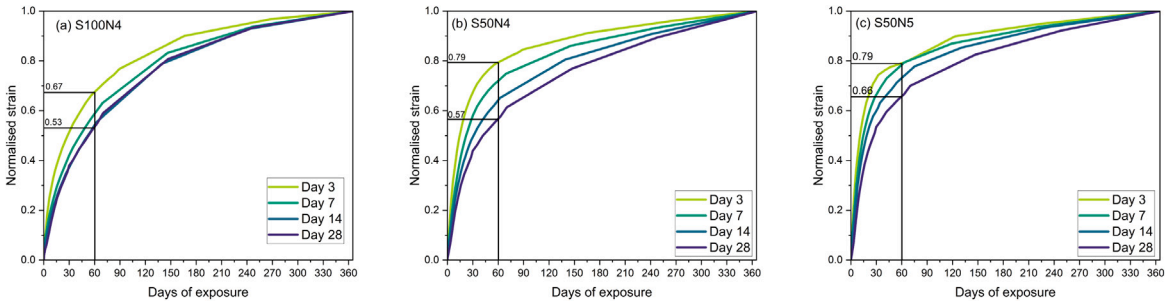

Fig. 8. Comparison of normalized strain for different mixes.

porosity data discussed in Section 3.3, the cumulative intrusion of the S100N4 after 14 days of sealed curing was 0.067 ml/gm, while it was higher for S50N4 with a value of 0.12 ml/gm. Fig. 8(c) shows the development of the shrinkage strain with higher alkali content (S50N5), which also shows a rapid increase in shrinkage strains at early ages. The S50N5 mix exhibits higher hydration kinetics compared to S50N4. Consequently, the effect of varying curing conditions on the normalized strain (ϵ_n) is less pronounced for S50N5.

To further elucidate the shrinkage kinetics, a differential analysis of the shrinkage data was performed. The shrinkage rate was calculated using a first-order finite difference approach, as given by:

$$\frac{d\epsilon}{dt} = \frac{\epsilon_{t+\Delta t} - \epsilon_t}{\Delta t} \tag{7}$$

where ϵ_t is the shrinkage strain at time t and Δt is the time interval between successive measurements. Fig. 9(a), (b), and (c) present the evolution of shrinkage rate ($\frac{d\epsilon}{dt}$) for S100N4, S50N4, and S50N5 mixtures exposed to drying after 3, 14, and 28 days of sealed curing, respectively. It is apparent from Fig. 9 that all the specimens exhibit a pronounced peak in shrinkage rate immediately after exposure, followed by a rapid decay and a long-term tail. The initial peak is significantly higher for specimens exposed to drying at early ages (3 days curing), indicating that shrinkage at this stage is primarily governed by rapid moisture loss and capillary stresses in a relatively coarse and weakly developed pore structure. Increasing the initial curing duration results in a significant reduction in the peak shrinkage rate and a smoother decay profile, indicating that a more developed and refined microstructure provides greater resistance to early-age deformation. It is evident from Fig. 9(a) that the S50N4 mixture consistently exhibits a higher shrinkage rate compared to S100N4 throughout the drying period. This behavior can be attributed to its relatively underdeveloped and weaker microstructure, as supported by the pore-size distribution results (Fig. 6). In contrast, the shrinkage rate of S50N5 remains comparable to that of S50N4, suggesting that although an increase in alkali content promotes reaction and densification, its influence on the shrinkage rate at early drying stages is less pronounced than that of the precursor composition. Furthermore, a comparison across Fig. 9(a), (b), and (c) reveals that the differences in shrinkage rate between the mixes progressively diminish with increasing initial curing duration. This trend indicates that prolonged curing leads to a more refined and homogenized microstructure, thereby reducing the sensitivity of shrinkage kinetics to variations in mix composition.

4.1.3. Shrinkage and mass loss

This section compares the shrinkage and mass loss characteristics, focusing on the effect of initial sealed curing, GGBS/FA ratio, and alkali content. Fig. 10(a) and (b) plots the shrinkage and mass loss curves for S100N4 and S50N4, respectively, for different initial sealed curing durations. The slope of the curves represents the shrinkage strain per unit mass loss. This property can be related to the susceptibility of the matrix to deform, given the similar amount of mass loss. It is evident that for the S100N4 mix (Fig. 10(a)), all the curves are close to each other, reflecting very little effect of the initial curing on the slope of the different lines. As discussed previously, the hydration of GGBS is rapid in the early ages; hence, less microstructure change happens with time. As a result of this, microstructure and matrix stiffness are relatively the same with time, hence the mass loss to shrinkage characteristics remains very similar with respect to initial curing time. For S50N4 mixes (Fig. 10(b)), as the hydration proceeds, a higher amount of water becomes bound in the gel phases, and therefore, less water remains free; consequently, lower mass loss occurs with a longer initial curing time for the S50N4. The slope of the lines in Fig. 10(b) decreases with higher initial curing time, indicating the matrix shows lower deformation at a similar amount of mass loss.

Fig. 11(a) and (b) plots the shrinkage and mass loss curves after 3 and 28 days, respectively, for different GGBS/FA ratios at the same alkali content. It is evident that for both initial sealed curing durations, the slope of the lines decreases with an increase in the FA content. Lower slope for the higher FA indicates that at the same mass loss, there will be lower shrinkage. This is also related to the dynamics of bound and free water in the hydrated paste for different systems. For higher GGBS, due to a higher hydration degree, the amount of free water is very little to evaporate in the drying environment. While it is also important to note that for curing days = 3, even at lower mass loss, shrinkage in S100N4 mix is the highest, reflecting a much refined pore structure. This is reflected in the pore size distribution data in Fig. 6(a). Due to this refined pore structure, capillary stresses are significantly higher compared to S70N4 and S50N4 mixes, causing higher shrinkage even at lower moisture loss.

Fig. 12(a) and (b) show the effect of alkali content on the shrinkage and mass loss characteristics for the S70 and S50 mixes, respectively. It is apparent that the mixes with higher alkali content have a lower mass loss for the same shrinkage, indicating they are less prone to water loss. This can also be linked to the higher bound water, resulting from a faster rate of hydration in mixes with higher alkali content, which leads to a higher formation of gels. Fig. 12(a) and (b) show higher slopes of the curves for the mix with higher alkali content, indicating that higher shrinkage occurs at similar moisture loss. It can also be observed that these differences in slopes for different alkali content are more prominent for less initial sealed curing durations.

It is also evident from Figs. 10–12 that the relationship between shrinkage and mass loss is not linear across all of the tested mixes. In the Figs. 10–12 all the curves exhibit a distinct S-shaped profile. During the initial stage, mass loss occurs with minimal shrinkage strain, indicating that early drying predominantly occurs from the coarse pores without causing significant capillary stresses. In the subsequent stage, shrinkage strain increases rapidly with mass loss, likely due to the progressive removal of capillary water, causing higher shrinkage. Finally, at later stages, the relationship between mass loss and shrinkage strain transitions to a more linear behavior. To quantitatively define the transitions between different stages, specific stage boundaries, inflection points, and stage-specific slopes were calculated. The boundaries — representing the mass-loss ranges where one stage transitions to the next — were determined using the tangent intersection method (see Appendix 6.1). Different parameters, such as the inflection point (m_0),

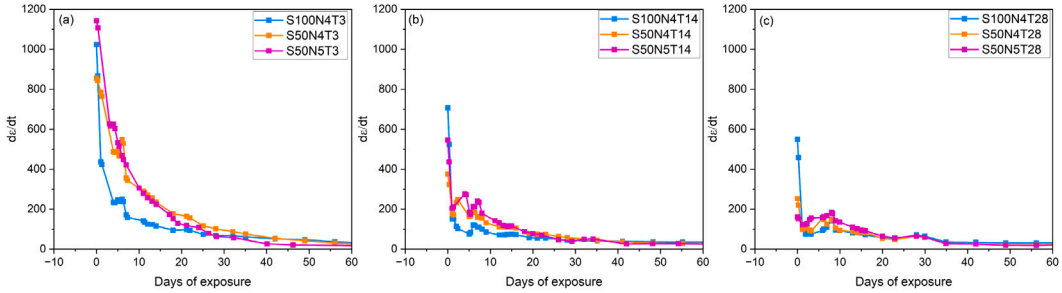

Fig. 9. Shrinkage rate of S100N4, S50N4, and S50N5 after different initial sealed curing days (a) 3 days, (b) 14 days and (c) 28 days.

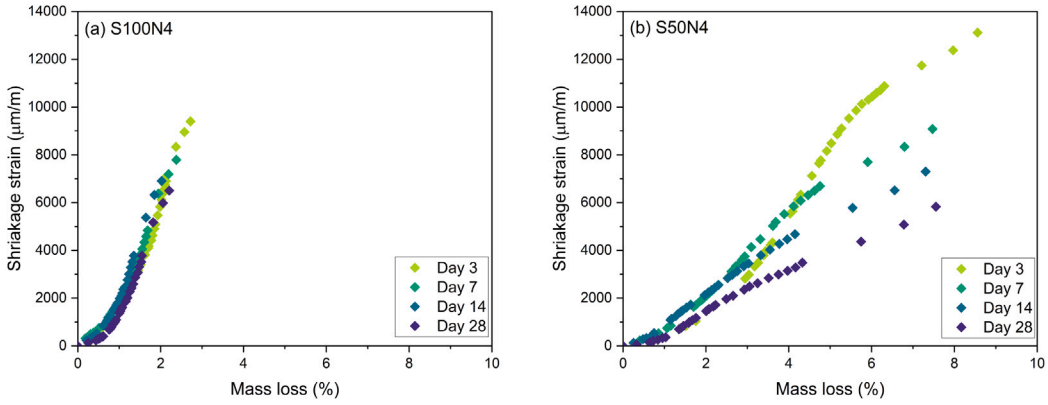

Fig. 10. Shrinkage and mass loss characteristic for mix with different initial curing time (a) for S100N4 (b) for S50N4.

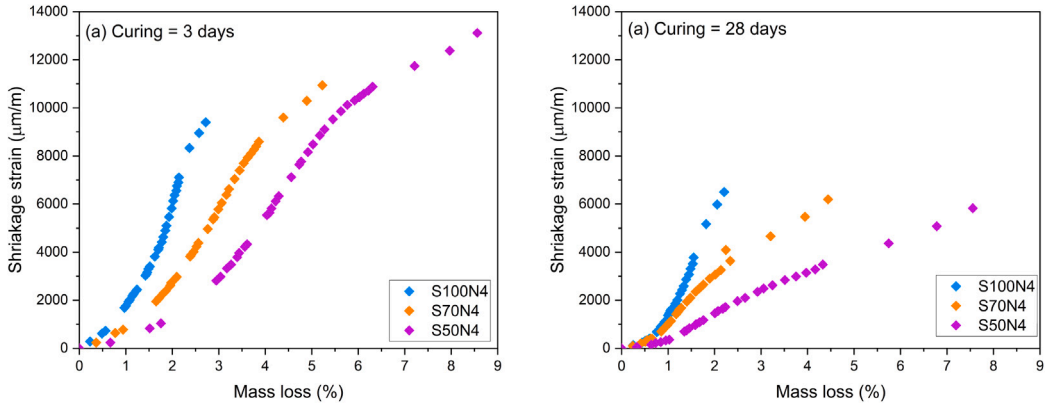

Fig. 11. Shrinkage and mass loss characteristic for mix with different GGBS/FA ratio (a) for 3 days of curing (b) for 28 days of curing.

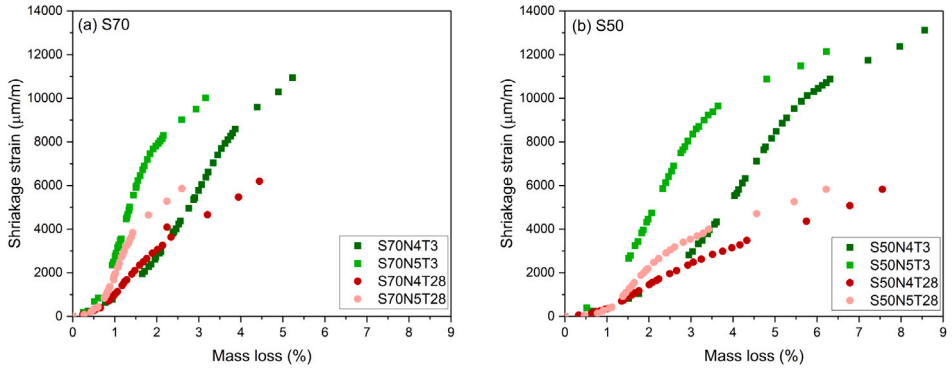

Fig. 12. Shrinkage and mass loss characteristic for mix with different alkali content (a) S70 (b) S50.

Table 3
Calculated inflection point and stage Boundaries for the shrinkage to mass-loss datasets for S100N4, S70N4, and S50N4.

	Parameters	S100N4				S70N4				S50N4			
		T3	T7	T14	T28	T3	T7	T14	T28	T3	T7	T14	T28
Inflection point	m_0	2.07	1.73	1.46	1.58	2.94	2.52	2.75	1.72	4.30	3.10	1.83	2.51
	ϵ_0	6557.1	5013.1	4253.1	3836.3	5643.6	4293.3	3583.0	2529.8	6340.3	4011.0	1962.0	1873.3
Slope	Stage 1 (Θ_1)	1255.9	1617.3	1092.0	520.7	829.2	677.3	427.9	491.1	553.8	593.8	572.6	228.8
	Stage 2 (Θ_2)	5644.0	5055.5	5599.5	5147.5	3405.5	2538.3	1819.6	2132.1	2889.4	1834.0	1232.5	921.2
	Stage 3 (Θ_3)	3030.7	3273.1	4034.3	3432.8	1583.3	1483.0	1381.2	1228.2	972.6	860.8	814.3	713.8
Stage boundaries	Stage 1-2 ($m12$)	1.22	1.09	0.87	0.93	1.68	1.14	1.02	0.70	2.59	1.34	0.44	0.63
	Stage 1-3 ($m13$)	2.48	2.11	1.71	1.88	3.83	3.37	3.09	2.04	5.64	4.37	3.75	3.73
	m_{max}	2.72	2.38	2.03	2.21	5.23	4.90	5.84	4.44	8.56	7.47	7.31	7.56
	ϵ_{max}	9398.1	7787.6	6905.2	6502.2	10 938.8	8745.4	8049.3	6193.7	13 117.3	9081.9	7297.0	5827.3
	$m12/m_{max}$	0.45	0.46	0.43	0.42	0.32	0.23	0.17	0.16	0.30	0.18	0.06	0.08
	$m23/m_{max}$	0.91	0.89	0.84	0.85	0.73	0.69	0.53	0.46	0.66	0.58	0.51	0.49

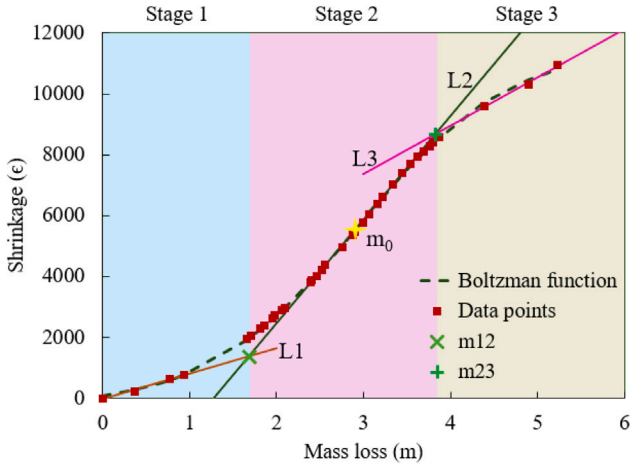

Fig. 13. Description of the different stages, stage boundaries, and inflection point for the S-curve.

stage boundaries (m12 and m23) and tangent line (L1, L2 and L3) are illustrated in Fig. 13, while the calculated values for all experimental series are summarized in Table 3 and 4. To compare different mixes, relative stage boundaries mass-loss (M_{ij}) is defined as given below:

$$M_{ij} = \frac{mij}{m_{max}} \tag{8}$$

Here mij is the mass loss at the stage boundary of i and j, and m_{max} is the maximum mass loss of the mix measured after 1 year. It can be observed from Table 3 that for S100N4, slopes for different stages are similar for different durations of initial curing time. While for S50N4, a clear decrement of the slopes with increase in curing times is observed (also reflected in Fig. 10). For S100N4, the $m12$ values usually range around 0.4, but they are lower for the S50N4. indicating that stage 2 starts at a lower relative mass loss for the mixes containing higher FA. Similarly, the transition from stage 2 to 3 also starts at a relative mass loss. The slope of the tangent lines is relatively higher for the mixes with higher slag and alkali content than for those with lower slag and alkali content, respectively. It is also clear from Tables 3 and 4 that the stage boundaries (m12 and m23) vary greatly with the mix design and initial curing durations. The normalized stage boundary m12 varies approximately from 0.06 to 0.46, while the transition from Stage 2 to Stage 3 (m23) occurs within a broader range of about 0.39 to 0.91. These wide ranges highlight the strong dependence of shrinkage–mass loss behavior on mix composition and initial curing conditions.

Research comparing the shrinkage behavior of Portland Cement (PC) and AAMs has revealed distinct relationships between mass loss and shrinkage strain. Specifically, a linear relationship is widely reported for PC systems [10,32], whereas the relationship between mass loss and shrinkage in AAMs is consistently found to be non-linear [10,19]. Ye and Aleksandra also conducted the shrinkage measurements for AAS at different RH and reported that the mass of the specimens becomes stable (i.e. approximately zero moisture loss) after a certain duration of drying, especially at very low RH [10]. In contrast, in the experiments conducted in the current study, the mass loss in all the specimens continues to occur till the end of the experiment (1 year), although the rate of mass loss becomes very slow with time.

4.2. Drying shrinkage in samples with comparable pore structure

This section addresses the mechanism governing drying shrinkage by isolating the influence of gel chemistry from pore structure effects. While the fundamental driving force for drying shrinkage is often attributed to deformation caused by capillary pressure, capillary pressure alone cannot account for the full magnitude of drying shrinkage observed in AAMs. The long-term evolution of drying shrinkage in alkali-activated FA and GGBS pastes is governed by the viscous behavior of the C-(N)-A-S-H gel, which is the main binding gel [16]. This viscous response is initiated by the high capillary pore pressures generated during curing due to self-desiccation and is further intensified during drying. Under sustained internal loading, the redistribution of capillary water and surface-adsorbed water progressively increases the stress carried by the gel's solid skeleton, leading to time-dependent viscous deformation of the gel. Similarly, Ye and Radlińska [10] demonstrated that the shrinkage kinetics of AAS are strongly influenced by the rearrangement and refinement of C-A-S-H gels under capillary pressure. Thus, structural changes in the gel at the nanoscale influence the deformations at the meso/macro scale. These nanoscale structural characteristics are largely determined by the compositional parameters of the gel (Ca/Si, Al/Si, Na/Si), which significantly influence gel stiffness and time-dependent behavior [16,58]. Isolating the specific contribution of gel compositional parameters to shrinkage behavior, therefore, requires controlling for pore structure variations.

In order to investigate the influence of gel chemistry on drying shrinkage, samples with comparable pore structures were identified and compared, ensuring that differences in shrinkage behavior could be attributed primarily to variations in gel characteristics. To enable a meaningful comparison of pore structure between different specimens, a criterion for comparable pore structure was established based on pore volumes obtained from MIP. Specifically, the pore volumes within two diameter ranges (2.5–10 nm and 10–58 nm) were calculated from the pore-size distribution. These ranges encompass both small gel pores and medium-sized capillary pores, which are known to play a key role in driving drying-induced deformation [59,60]. Two mixtures were considered to have comparable pore structures only when the difference in pore volume was less than 4.0% in both ranges simultaneously. If this condition was not satisfied in either range, the pore structures were not classified as comparable. Based on the above comparisons, two pairs of samples, namely S100N4T3 and S70N4T14 (named as Pair-1 in this

Table 4
Calculated inflection point and stage boundaries for the shrinkage to mass-loss datasets for S70N5 and S50N5.

	Parameters	S70N5				S50N5			
		T3	T7	T14	T28	T3	T7	T14	T28
Inflection point	m_0	1.28	0.95	0.97	1.17	2.23	1.76	1.04	2.05
	ϵ_0	4466.69	3376.81	2869.96	2664.73	5394.94	3677.92	2012.58	2167.07
Slope	Stage 1 (Θ_1)	1332.07	1428.24	992.11	467.60	1824.52	816.58	801.39	177.82
	Stage 2 (Θ_2)	6122.01	5851.69	5361.01	4795.71	3891.29	3158.76	2554.71	1688.30
	Stage 3 (Θ_3)	1729.97	1644.45	1829.01	1517.00	880.36	773.15	639.51	672.62
Stage boundaries	Stage 1-2 ($m12$)	0.70	0.50	0.53	0.68	1.48	0.80	0.36	0.85
	Stage 1-3 ($m13$)	1.80	1.32	1.27	1.48	3.29	2.73	2.07	2.88
	m_{max}	3.16	2.60	2.27	2.60	6.22	5.72	5.25	6.22
	ϵ_{max}	10 015.51	7692.63	6356.83	5857.62	12 142.52	9072.68	6706.90	5825.35
	$m12/m_{max}$	0.22	0.19	0.23	0.26	0.24	0.14	0.07	0.14
	$m23/m_{max}$	0.57	0.51	0.56	0.57	0.53	0.48	0.39	0.46

article), as well as S70N4T7 and S50N5T3 (named as Pair-2 in this article), showed comparable pore structures, with similar differential pore size distribution curves (as shown in Fig. 14 (a1, a2) and (b1, b2). By ensuring similarity in pore size distribution within these critical ranges, the influence of pore structure on shrinkage can be effectively controlled. However, due to the inherent pressure limitations and technical constraints of the MIP technique, specifically the 'ink-bottle', some pores within the 2.5–10 nm range, and particularly those smaller than 2.5 nm, cannot be fully intruded by mercury, thus posing challenges in capturing the full distribution of finer pores [61,62]. Notably, the MIP data presented here are intended for comparative analysis between samples rather than an absolute pore characterization. Pores falling below the 2.5 nm threshold are excluded from the comparison criteria of the comparable pore structure, as they typically correspond to the interlayer spacing of the gel phase. Such dimensions are considered inherent characteristics of the C-N-A-S-H gel rather than the capillary pore network. Hence, pore sizes below 2.5 nm are considered part of the gel characteristics in this work. Consequently, the observed differences in shrinkage and mass loss behavior of the samples can be attributed to variations in the composition and structure of their gel phases [14].

Despite the similarities in pore characteristics, the comparable samples showed significantly different drying shrinkage and mass loss behaviors (Fig. 15). Over the 365-day exposure period, S100N4T3 exhibits considerably greater drying shrinkage but lower weight loss compared to S70N4T14. In contrast, S50N5T3 shows both higher drying shrinkage and greater weight loss than S70N4T7. These findings are consistent with previous literature, which reports that drying shrinkage and mass loss do not necessarily correlate [34].

To better understand the underlying mechanisms of drying shrinkage and mass loss behavior, the selected specimens were analyzed using SEM-EDS. Representative SEM micrographs of these specimens are presented in Fig. 16, and Table 5 presents the corresponding average elemental ratios (Ca/Si, Al/Si, Na/Si) and the estimated volumes of the reaction products. These compositional parameters are selected due to their direct influence on gel nanostructure [40,41] which in turn, governs drying shrinkage behavior. Notably, the pore structure and SEM-EDS analyses presented in this study correspond to a specific age prior to drying exposure and therefore reflect the initial microstructure and gel composition at the onset of drying. The comparisons made between selected mixtures with comparable pore structures are intended to isolate the influence of gel composition on shrinkage behavior at early ages, particularly in terms of shrinkage rate immediately after exposure. However, both pore structure and gel composition are expected to evolve with ongoing reaction and drying. Therefore, the interpretation of gel chemistry effects based on SEM-EDS is limited to the shrinkage rate just after exposure to drying conditions and not for long-term drying shrinkage.

As shown in Table 5, specimens in Pair 1 and Pair 2 show notable differences in Ca/Si and Na/Si ratios. However, the Al/Si ratio remains relatively consistent. The measured elemental ratios, showing Ca/(Si+Al) ratios below 1.2 (Table 5), suggest the development of C-(N)-A-S-H gel phases in the samples [63–65]. This interpretation aligns with EDS findings reported in previous studies on AAS and GGBS-blended pastes [66–70]. Moreover, a general comparison of samples in Table 5 indicates that samples with higher GGBS content tend to form a greater quantity of reaction products, regardless of curing time or alkali content. This is particularly evident in S100N4T3, which exhibits the highest reaction product content at approximately 70%. As explained earlier, the higher formation of reaction products in GGBS-rich samples is mainly due to the high reactivity and calcium availability of GGBS, which promotes more extensive gel formation [38].

Fig. 17 illustrates the atomic ratios of Ca/Si and Na/Si obtained through SEM-EDS for selected comparable samples. A comparison between the specimens of Pair 1 (S100N4T3 vs. S70N4T14) reveals that gels in S100N4T3 have a higher mean Ca/Si ratio (1.06) compared to S70N4T14 (Ca/Si = 0.88). This higher Ca/Si ratio enhances the water-retaining capacity, which results in the reduced moisture loss as observed in S100N4T3 (Fig. 15) [42]. Moreover, the greater quantity of reaction products formed in this sample contributes to lower mass loss [23]. However, the higher drying shrinkage observed in S100N4T3 (Fig. 15) can be linked to the high Na/Si ratio of this sample (Fig. 17). C-(N)-A-S-H gels with higher Na/Si ratios tend to exhibit increased drying shrinkage due to their lower degree of polymerization, shorter silicate chain lengths, and greater interlayer spacing [63]. Similarly, the structural incorporation of alkali (Na and K) cations into C-A-S-H gels has also been shown to disrupt the stacking regularity of the gel layers, thereby making the network more susceptible to collapse and redistribution during drying [10,15]. Hence, the extra alkalis in the composition of the reaction products negatively influence the shrinkage behavior [34] by changing the nanostructure of gels. A similar behavior is observed in the specimens of Pair 2, S70N4T7 and S50N5T3, when comparing their shrinkage and mass loss behavior (Fig. 15) with their compositional characteristics (Table 5). Although both mixtures present comparable pore sizes, S70N4T7 demonstrates a lower degree of mass loss, which is likely associated with its higher Ca/Si ratio and the increased formation of reaction products. Furthermore, the decreased shrinkage rate observed in S70N4T7 may be attributed to its lower Na/Si ratio compared to S50N5T3. These findings further confirm the influence of the Ca/Si ratio and reaction product content on water retention capacity and the role of the Na/Si ratio in shrinkage susceptibility. Moreover, as the Al/Si ratio is almost comparable among samples (Table 5), no significant differences in the formation of Al-containing secondary phases are expected, and the extent of Al incorporation into the gel network is likely comparable across the samples [71].

In summary, this comprehensive study advances the understanding of drying shrinkage in AAMs by systematically evaluating the effects of mix-design parameters, initial sealed curing duration, and pore structure, and further decouples it to understand the effect of gel chemistry on long-term shrinkage measurements. The long-term measurements

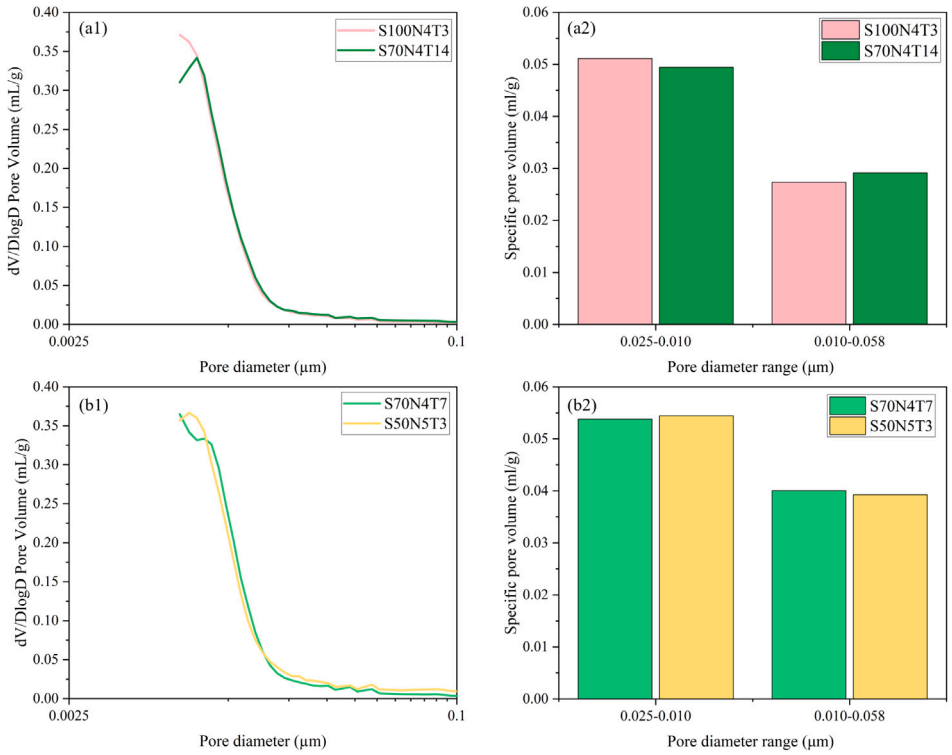

Fig. 14. Differential pore size distribution (a1 and b1) and corresponding specific pore volume within pore diameter ranges (a2 and b2) for two comparable sample pairs: S100N4T3 vs. S70N4T14 and S70N4T7 vs. S50N5T3.

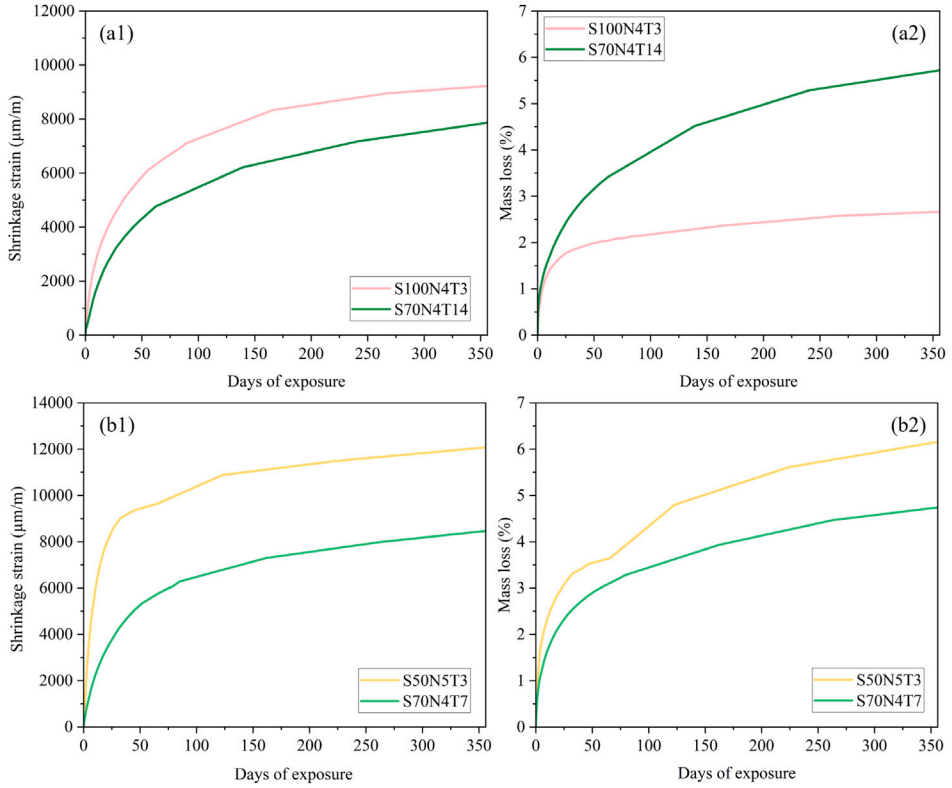

Fig. 15. Differential pore size distribution (a1 and b1) and corresponding specific pore volume within pore diameter ranges (a2 and b2) for two comparable sample pairs: S100N4T3 vs. S70N4T14 and S70N4T7 vs. S50N5T3.

reveal that the kinetics and magnitude of shrinkage are strongly influenced by early-age exposure conditions. Crucially, it resolves the discrepancy in the current literature regarding which mix formulation exhibits the highest susceptibility to long-term shrinkage [29–31]. If the

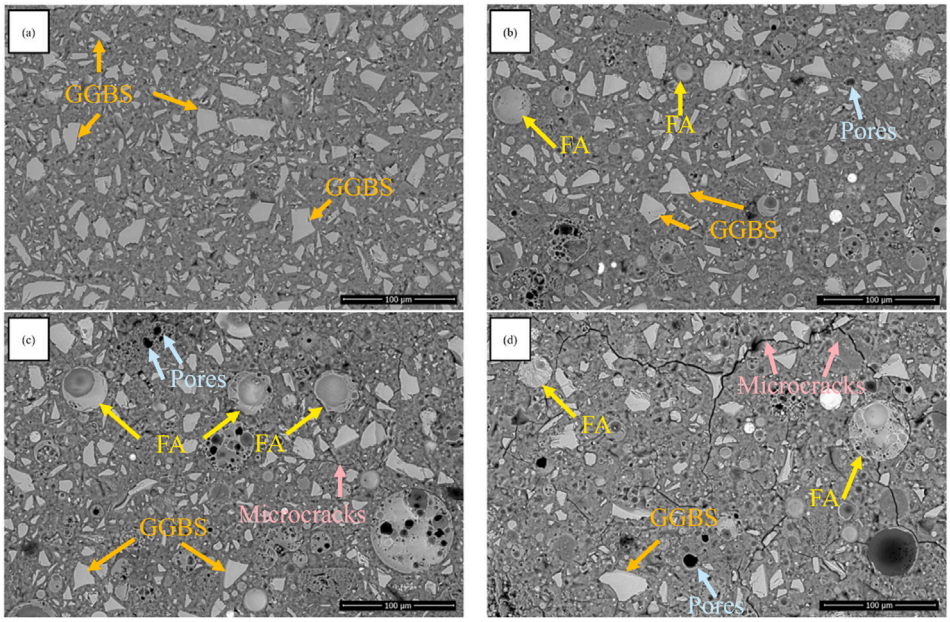

Fig. 16. SEM micrographs of selected samples (a) S100N4T3, (b) S70N4T14, (c) S70N4T7, and (d) S50N5T3, highlighting differences in microstructural compactness, unreacted GGBS and FA particles, and the presence of pores and microcracks..

Table 5
Mean atomic ratios and amount of reaction products.

Pair	Sample name	Ca/Si	Al/Si	Na/Si	Ca/(Si+Al)	Amount of reaction products (%)
Pair 1	S100N4T3	1.06	0.30	0.34	0.81	70.1
	S70N4T14	0.89	0.31	0.24	0.68	59.5
Pair 2	S70N4T7	0.87	0.31	0.26	0.67	55.3
	S50N5T3	0.71	0.30	0.30	0.55	33.1

*Values were calculated using a 10% trimmed mean to reduce the influence of outliers (5% of values removed from each end of the data distribution).

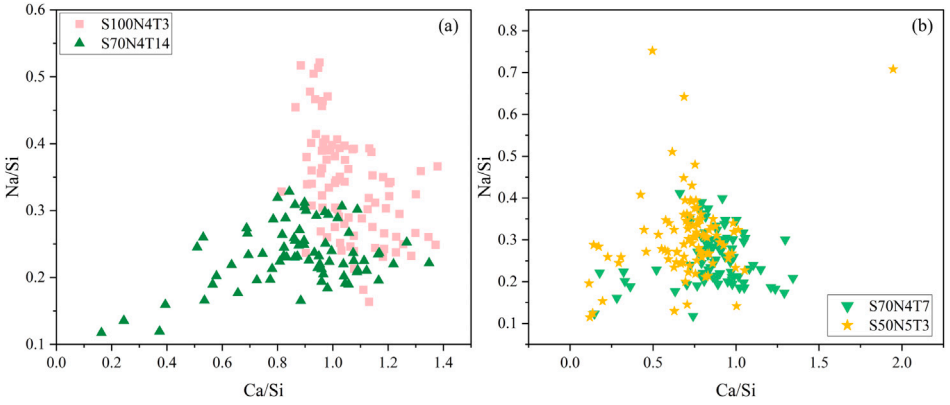

Fig. 17. Atomic Ca/Si and Na/Si ratios obtained from SEM-EDS analysis for (a) Pair 1: S100N4T3 vs. S70N4T14 and (b) Pair 2: S70N4T7 vs. S50N5T3.

AAMs are cured for shorter durations (such as 3 days) before exposure to driving environments, AAMs with higher FA content will be more prone to shrinkage; in contrast, if cured for a sufficient duration (such as 28 days), AAMs with higher GGBS content will result in the higher shrinkage strains. Long-term measurements are crucial, specifically for mixes with higher GGBS content, which show slower shrinkage kinetics and shrinkage could only reach 53%–67% (in 60 days) of the final shrinkage after 1 year.

Beyond resolving the role of curing duration and mix composition, this study clarifies the role of compositional parameters (Ca/Si, Al/Si, and Na/Si ratios) on shrinkage behavior, as these parameters influence shrinkage through two interrelated pathways: modification of pore structure and alteration of gel nanostructure. By identifying sample pairs with comparable pore structures but differing gel compositions, this work isolated the gel-controlled mechanism and demonstrates that the Na/Si ratio of the gels within the microstructure is a key parameter influencing shrinkage susceptibility independent of pore structure effects. While higher Ca/Si ratios improved water retention and pore refinement, the accompanying increase in Na/Si ratio increases shrinkage susceptibility through gel-level mechanisms. While the present study provides insights into the influence of mix design, curing conditions, and gel characteristics on the long-term drying shrinkage of AAMs, a more detailed understanding of the underlying mechanisms, particularly the transition between early-age and late-age shrinkage behavior,

requires further investigation. Specifically, the relative contributions of capillary stresses, disjoining pressure, and gel-level deformation need to be clearly understood. In addition, although SEM-EDS enables targeted characterization of gel composition within selected regions, a more comprehensive understanding of the aluminosilicate network connectivity would benefit from advanced structural characterization techniques such as Si and Al- NMR. Since in the current study, MIP is used to quantify the pore structure of the AAMs, which has limitations due to the ink bottle effect, and for quantifying pores below 2.5 nm. Hence, nitrogen sorption and proton NMR should be explored to better capture the pore structure of the AAMs. Such an approach would enable a more rigorous identification of the dominant driving mechanisms at different stages of drying and provide a deeper mechanistic framework for predicting long-term shrinkage in AAMs. This improved understanding will also help development of multiphysics models incorporating moisture transport, capillary stress evolution, and gel-level deformation to be calibrated and validated.

5. Conclusions

In this work, a comprehensive set of dedicated experiments has been performed to study the drying shrinkage behaviors of AAMs. This study highlights the effect of the mix design parameters of AAMs, such as the GGBS/FA ratio, alkali content, and curing conditions, on the long-term drying shrinkage and its kinetics. Further, the pore structures of various AAM specimens were analyzed to identify those with similar pore structures, enabling a focused examination of how gel characteristics affect drying shrinkage. The major conclusions from the current study are as follows:

(1) For all the mixes of AAMs used in the current study, a higher initial sealed curing time has drastically reduced drying shrinkage. However, the standard 60-day exposure period captured only 53%–66% of the one-year shrinkage in specimens cured for 28 days, demonstrating that short-term measurements alone are insufficient for evaluating the long-term shrinkage behavior specifically for AAMs.
(2) At early ages (short curing durations), shrinkage is primarily controlled by microstructural resistance. Mixtures with higher FA content exhibit up to 12870 μm/m shrinkage due to their relatively weak and porous microstructure. Conversely, after 28 days of curing, the trend reversed, and the 100% GGBS mix (S100N4) exhibited higher drying shrinkage than the 50% FA mix (S50N4), due to its extremely fine pore structure, which generated high capillary stresses.
(3) Due to more extensive geopolymerization reaction which increases the amount of reaction products, mixes with higher alkali content have mitigated shrinkage across different blends; for instance, one-year shrinkage decreased from 10,500 μm/m to 9500 μm/m for S70 mixes and from 12,500 μm/m to 11,500 μm/m for S50 mixes.
(4) Higher FA or alkali content in AAMs both lead to faster shrinkage kinetics. Consequently, these mixes exhibit rapid attainment of the ultimate shrinkage strain, reaching that state in a shorter timeframe than mixes with lower FA and alkali content. Specifically, the normalized shrinkage strain at 60 days for the S50N4 mix exposed at 3 days was 0.79, compared to 0.67 for the S100N4 mix under the same conditions.
(5) Shrinkage and mass loss curves for all the specimens do not follow a linear relationship but reflect an S-curve relationship where the shrinkage and mass loss occur in three stages. AAMs with higher GGBS and higher alkali show a steeper slope in the shrinkage and mass loss curves, indicating greater shrinkage and lower water loss due to the greater amount of bound water in similar conditions. The transition between different stages varies significantly with the mix design, normalized mass loss stage limits range from 0.06–0.46 (Stage 1–2) and 0.39–0.91 (Stage 2–3).
(6) By isolating samples with comparable pore structures, it was determined that gel chemistry directly dictates volumetric stability: a higher mean Ca/Si ratio (1.06 vs 0.88) and a larger volume of reaction products (70.1% vs 59.5%) improved water retention and reduced mass loss. However, an increased Na/Si ratio (0.34 vs 0.24) was found to disrupt the C-(N)-A-S-H gel network, increasing susceptibility to drying shrinkage regardless of pore refinement.

CRediT authorship contribution statement

Mayank Gupta: Writing – original draft, Visualization, Supervision, Methodology, Investigation, Formal analysis, Data curation, Conceptualization. **Farnaz Aghabeyk:** Writing – original draft, Visualization, Methodology, Investigation, Formal analysis, Data curation, Conceptualization. **Christa Winterman:** Writing – review & editing, Visualization, Methodology, Investigation, Formal analysis, Data curation, Conceptualization. **Guang Ye:** Writing – review & editing, Supervision, Conceptualization.

Declaration of competing interest

The authors declare that they have no known competing financial interests or personal relationships that could have appeared to influence the work reported in this paper.

Appendix 6

6.1. Determination of inflection point and stage boundaries by tangent intersection

To calculate the inflection point for the S- curve between the mass-loss (m) and the shrinkage strain (ϵ), a four-parameter Boltzmann (logistic) function was fitted to each dataset.

$$\epsilon = A_2 + \frac{A_1 - A_2}{1 + e^{(m-m_0)/dm}} \tag{9}$$

where (A_1) and (A_2) are upper and lower asymptotes, (m_0) is the inflection abscissa, and (dm) controls the slope width. The inflection point is analytically at ($m = m_0$); its ordinate is (ϵ). The tangent (Stage 2 line) at the inflection has slope (Θ_2):

$$\Theta_2 = -\frac{A_1 - A_2}{4, d_m} \tag{10}$$

The tangent line (L_2) is derived from the inflection point and slope (Θ_2). For the stage 1 and stage 3 baseline segments (L_1 and L_3), simple linear regressions were defined by the first three and last three observed points, respectively. These calculations will provide three tangent lines (one for each stage). Stage boundaries are estimated from intersection points of the L_1, L_2, and L_3.

Data availability

Data will be made available on request.

References

[1] C. Shi, B. Qu, J.L. Provis, Recent progress in low-carbon binders, Cem. Concr. Res. 122 (2019) 227–250.
[2] G. Habert, S.A. Miller, V.M. John, J.L. Provis, A. Favier, A. Horvath, K.L. Scrivener, Environmental impacts and decarbonization strategies in the cement and concrete industries, Nat. Rev. Earth & Environ. 1 (11) (2020) 559–573.
[3] M. Gupta, S.H. Hajiabadi, F. Aghabeyk, Y. Chen, R. van Noort, M. Khalifeh, G. Ye, Understanding microstructural changes of a one-part geopolymer exposed to CO2 for geological carbon storage application–an experimental and numerical investigation, Carbon Capture Sci. Technol. (2025) 100466.
[4] B. Zhang, J. Cao, C. You, Z. Yang, H. Peng, Multi-scale insights into the distinctive toughening mechanisms of basalt fibers in seawater sea-sand geopolymer composites, Compos. Part B: Eng. (2025) 113290.

[5] B. Zhang, H. Zhu, P. Feng, P. Zhang, A review on shrinkage-reducing methods and mechanisms of alkali-activated/geopolymer systems: Effects of chemical additives, J. Build. Eng. 49 (2022) 104056.
[6] P. Rovnaník, I. Kusák, P. Bayer, P. Schmid, L. Fiala, Comparison of electrical and self-sensing properties of Portland cement and alkali-activated slag mortars, Cem. Concr. Res. 118 (2019) 84–91.
[7] W.J. Weiss, S.P. Shah, Restrained shrinkage cracking: the role of shrinkage reducing admixtures and specimen geometry, Mater. Struct. 35 (2) (2002) 85–91.
[8] H. Ye, A. Radlińska, A review and comparative study of existing shrinkage prediction models for portland and non-portland cementitious materials, Adv. Mater. Sci. Eng. 2016 (1) (2016) 2418219.
[9] J. Yang, Q. Wang, Y. Zhou, Influence of curing time on the drying shrinkage of concretes with different binders and water-to-binder ratios, Adv. Mater. Sci. Eng. 2017 (1) (2017) 2695435.
[10] H. Ye, A. Radlińska, Shrinkage mechanisms of alkali-activated slag, Cem. Concr. Res. 88 (2016) 126–135.
[11] B. Singh, M.R. Rahman, R. Paswan, S. Bhattacharyya, Effect of activator concentration on the strength, ITZ and drying shrinkage of fly ash/slag geopolymer concrete, Constr. Build. Mater. 118 (2016) 171–179.
[12] X. Hu, C. Shi, X. Liu, Z. Zhang, Studying the effect of alkali dosage on microstructure development of alkali-activated slag pastes by electrical impedance spectroscopy (EIS), Constr. Build. Mater. 261 (2020) 119982.
[13] N. Lee, J.G. Jang, H.-K. Lee, Shrinkage characteristics of alkali-activated fly ash/slag paste and mortar at early ages, Cem. Concr. Compos. 53 (2014) 239–248.
[14] M. Mastali, P. Kinnunen, A. Dalvand, R.M. Firouz, M. Illikainen, Drying shrinkage in alkali-activated binders–a critical review, Constr. Build. Mater. 190 (2018) 533–550.
[15] B. Zhang, H. Zhu, Y. Cheng, G.F. Huseien, K.W. Shah, Shrinkage mechanisms and shrinkage-mitigating strategies of alkali-activated slag composites: A critical review, Constr. Build. Mater. 318 (2022) 125993.
[16] D. Huang, P. Chen, H. Peng, Q. Yuan, X. Tian, Drying shrinkage performance of medium-Ca alkali-activated fly ash and slag pastes, Cem. Concr. Compos. 130 (2022) 104536.
[17] F. Collins, J.G. Sanjayan, Effect of pore size distribution on drying shrinking of alkali-activated slag concrete, Cem. Concr. Res. 30 (9) (2000) 1401–1406.
[18] X. Hu, C. Shi, Z. Shi, L. Zhang, Compressive strength, pore structure and chloride transport properties of alkali-activated slag/fly ash mortars, Cem. Concr. Compos. 104 (2019) 103392.
[19] H. Ye, A. Radlińska, Shrinkage mitigation strategies in alkali-activated slag, Cem. Concr. Res. 101 (2017) 131–143.
[20] M. Gupta, K. Pen, G. Igarashi, Y. Takahashi, T. Ishida, Effect of reinforcement on the anisotropic expansion of concrete with CSA-based expansive additives, J. Build. Eng. 97 (2024) 110740.
[21] M. Gupta, K. Pen, G. Igarashi, Y. Takahashi, T. Ishida, Expansion characteristics of concrete with free lime based expansive additives under uniaxial restraint conditions, Constr. Build. Mater. 356 (2022) 129330.
[22] M. Gupta, G. Igarashi, Y. Takahashi, T. Ishida, Multiscale chemo-mechanical modeling of concrete expansion with free lime-based expansive additives under restraint conditions, Cem. Concr. Compos. 141 (2023) 105126.
[23] B. Akturk, A.B. Kizilkanat, Improvement of durability and drying shrinkage of sodium carbonate activated slag through the incorporation of calcium hydroxide and sodium hydroxide, Constr. Build. Mater. 243 (2020) 118260.
[24] M. Alonso, S. Gismera, M. Blanco, M. Lanzón, F. Puertas, Alkali-activated mortars: Workability and rheological behaviour, Constr. Build. Mater. 145 (2017) 576–587.
[25] H. Gao, I.M.A. Al-Damad, A. Siddika, T. Kim, S. Foster, A. Hajimohammadi, Enhancing the workability retention of one-part alkali activated binders by adjusting the chemistry of the activators, Cem. Concr. Compos. 157 (2025) 105928.
[26] M. Gupta, X. Qiu, M. Omran, Y. Chen, M. Khalifeh, G. Ye, Reaction and microstructure development of one-part geopolymer for wellbore applications–an experimental and numerical study, Cem. Concr. Res. 188 (2025) 107738.
[27] Y. Chen, J. Chen, M. Gupta, X. Liang, L.M. de Lima, Z. Xu, Y. Zuo, S. Yin, Q. Yu, G. Ye, An experimental and numerical study of alkali-activated fly ash paste–from dissolution kinetics to microstructure formation, Cem. Concr. Res. 198 (2025) 107999.
[28] Z. Jiao, S. Zhang, Y. Wang, Z. Dong, Z. Lu, Influence of fly ash content on pore structure regulation in alkali-activated slag under alkaline conditions, Constr. Build. Mater. 485 (2025) 141863.
[29] W. Shen, Y. Wang, T. Zhang, M. Zhou, J. Li, X. Cui, Magnesia modification of alkali-activated slag fly ash cement, J. Wuhan Univ. Technology-Mater. Sci. Ed. 26 (2011) 121–125.
[30] A.M. Rashad, Properties of alkali-activated fly ash concrete blended with slag, Iran. J. Mater. Sci. Eng. 10 (1) (2013) 57–64.
[31] G. Wang, Y. Ma, Drying shrinkage of alkali-activated fly ash/slag blended system, J. Sustain. Cement-Based Mater. 7 (4) (2018) 203–213.
[32] Y. Ma, G. Ye, The shrinkage of alkali activated fly ash, Cem. Concr. Res. 68 (2015) 75–82.
[33] G. Samson, M. Cyr, X.X. Gao, Formulation and characterization of blended alkali-activated materials based on flash-calcined metakaolin, fly ash and GGBS, Constr. Build. Mater. 144 (2017) 50–64.
[34] M. Hanumananaik, K.V. Subramaniam, Shrinkage in low-calcium fly ash geopolymers for precast applications: Reaction product content and pore structure under drying conditions, J. Build. Eng. 78 (2023) 107583.
[35] I. Garcia-Lodeiro, A. Palomo, A. Fernández-Jiménez, An overview of the chemistry of alkali-activated cement-based binders, in: Handbook of Alkali-Activated Cements, Mortars and Concretes, Elsevier, 2015, pp. 19–47.
[36] B. Walkley, R. San Nicolas, M.-A. Sani, G.J. Rees, J.V. Hanna, J.S. van Deventer, J.L. Provis, Phase evolution of C-(n)-ASH/NASH gel blends investigated via alkali-activation of synthetic calcium aluminosilicate precursors, Cem. Concr. Res. 89 (2016) 120–135.
[37] Y. Tao, K. Sun, J. Yang, B. Shen, Y. Zhang, D. Hui, Influence of calcium oxide and sodium silicate on the setting, hardening and shrinkage properties of alkali-activated slag/fly ash mortars, Constr. Build. Mater. 453 (2024) 139104.
[38] N. Lee, H.-K. Lee, Reactivity and reaction products of alkali-activated, fly ash/slag paste, Constr. Build. Mater. 81 (2015) 303–312.
[39] T.A. Aiken, J. Kwasny, W. Sha, M.N. Soutsos, Effect of slag content and activator dosage on the resistance of fly ash geopolymer binders to sulfuric acid attack, Cem. Concr. Res. 111 (2018) 23–40.
[40] D.-W. Zhang, T.-T. Yang, X.-G. Xu, Y.-R. Wang, H. Li, Relationship between MO/(SiO2+ Al2O3) of materials—amorphous gel structure—properties of the one-part FA-Slag-based AAMs, J. Environ. Chem. Eng. 12 (6) (2024) 114519.
[41] Y. Ma, B. Wang, C. Zhang, X. Lin, Y. Yang, Z. Chen, T. Ji, Relationship of drying shrinkage and the bond strength between alkali-activated steel slag/fly ash lightweight mortar and concrete substrate: Phase assemblage and micro-mechanical property, J. Build. Eng. 99 (2025) 111587.
[42] X. Zhu, D. Tang, K. Yang, Z. Zhang, Q. Li, Q. Pan, C. Yang, Effect of Ca (OH) 2 on shrinkage characteristics and microstructures of alkali-activated slag concrete, Constr. Build. Mater. 175 (2018) 467–482.
[43] L. Luo, W. Yao, G. Liang, Y. Luo, Workability, autogenous shrinkage and microstructure of alkali-activated slag/fly ash slurries: Effect of precursor composition and sodium silicate modulus, J. Build. Eng. 73 (2023) 106712.
[44] C. Kuenzel, L.J. Vandeperre, S. Donatello, A.R. Boccaccini, C. Cheeseman, Ambient temperature drying shrinkage and cracking in metakaolin-based geopolymers, J. Am. Ceram. Soc. 95 (10) (2012) 3270–3277.
[45] K. Guo, H. Dong, J. Zhang, L. Zhang, Z. Li, Experimental study of alkali-activated cementitious materials using thermally activated red mud: effect of the Si/Al ratio on fresh and mechanical properties, Buildings 15 (4) (2025) 565.
[46] T. Yang, H. Zhu, Z. Zhang, Influence of fly ash on the pore structure and shrinkage characteristics of metakaolin-based geopolymer pastes and mortars, Constr. Build. Mater. 153 (2017) 284–293.
[47] J. Ban, K. Sun, J.-X. Lu, H.A. Ali, J. Yao, G. Sunahara, C.-S. Poon, Effect of air pollution-controlled residue of a sewage sludge incinerator on the drying shrinkage and the pore structure of alkali-activated materials, Waste Manage. 161 (2023) 178–186.
[48] K. Li, Z. Yang, D. Nicolaides, M. Liang, B. Briseghella, G.C. Marano, Y. Zhang, Autogenous shrinkage and sustainability assessment of alkali-activated slag incorporating steel slag, Constr. Build. Mater. 438 (2024) 137219.
[49] D. Huang, Q. Yuan, P. Chen, X. Tian, H. Peng, Effect of activator properties on drying shrinkage of alkali-activated fly ash and slag, J. Build. Eng. 62 (2022) 105341.
[50] B. Chen, Utilization of MSWI bottom ash as a mineral resource for low-carbon construction materials: quality-upgrade treatments, mix design method, and microstructure analysis, 2023.
[51] B. Sun, Y. Sun, G. Ye, G. De Schutter, A mix design methodology of slag and fly ash-based alkali-activated paste, Cem. Concr. Compos. 126 (2022) 104368.
[52] M. Nedeljković, Z. Li, G. Ye, Setting, strength, and autogenous shrinkage of alkali-activated fly ash and slag pastes: Effect of slag content, Materials 11 (11) (2018) 2121.
[53] S. Berg, D. Kutra, T. Kroeger, C.N. Straehle, B.X. Kausler, C. Haubold, M. Schiegg, J. Ales, T. Beier, M. Rudy, et al., Ilastik: interactive machine learning for (bio) image analysis, Nature Methods 16 (12) (2019) 1226–1232.
[54] N. Marjanović, M. Komljenović, Z. Baščarević, V. Nikolić, R. Petrović, Physical–mechanical and microstructural properties of alkali-activated fly ash–blast furnace slag blends, Ceram. Int. 41 (1) (2015) 1421–1435.
[55] V.M. Lima, P.A. Basto, M.A. Henrique, Y.M. Almeida, A.A. de Melo Neto, Optimizing the concentration of Na2O in alkaline activators to improve mechanical properties and reduce costs and CO2 emissions in alkali-activated mixtures, Constr. Build. Mater. 344 (2022) 128185.
[56] G.W. Scherer, Theory of drying, J. Am. Ceram. Soc. 73 (1) (1990) 3–14.
[57] S.F. Rahman, Z.C. Grasley, The significance of pore liquid pressure and disjoining pressure on the desiccation shrinkage of cementitious materials, Int. J. Adv. Eng. Sci. Appl. Math. 9 (2) (2017) 87–96.
[58] Z. Jia, R. Cao, S. Zhang, Y. Gao, C. Chen, Y. Zhang, Revealing the difference between creep behavior of hydration products of portland cement and alkali-activated slag paste at early age, J. Build. Eng. 77 (2023) 107556.
[59] G. Ye, Experimental study and numerical simulation of the development of the microstructure and permeability of cementious materials, 2003.

[60] Y. Guo, J. Qian, X. Wang, Pore structure and influence of recycled aggregate concrete on drying shrinkage, Math. Probl. Eng. 2013 (1) (2013) 912412.
[61] A. Muller, K. Scrivener, A reassessment of mercury intrusion porosimetry by comparison with 1h NMR relaxometry, Cem. Concr. Res. 100 (2017) 350–360.
[62] Y. Ma, G. Wang, G. Ye, J. Hu, A comparative study on the pore structure of alkali-activated fly ash evaluated by mercury intrusion porosimetry, N2 adsorption and image analysis, J. Mater. Sci. 53 (8) (2018) 5958–5972.
[63] R. Jia, Q. Wang, T. Luo, Investigation of the relationship among the hydration, microstructure and compressive strength of alkali-activated phosphorus slag, J. Build. Eng. 76 (2023) 107293.
[64] M.R. Ahmad, L.-P. Qian, Y. Fang, A. Wang, J.-G. Dai, A multiscale study on gel composition of hybrid alkali-activated materials partially utilizing air pollution control residue as an activator, Cem. Concr. Compos. 136 (2023) 104856.
[65] C. Liu, Z. Li, S. Nie, J. Skibsted, G. Ye, Structural evolution of calcium sodium aluminosilicate hydrate (C-(N-) ASH) gels induced by water exposure: the impact of Na leaching, Cem. Concr. Res. 178 (2024) 107432.
[66] H.A. Ali, K. Sun, D. Xuan, J.-X. Lu, M. Cyr, C.S. Poon, Recycling of high-volume waste glass powder in alkali-activated materials: An efflorescence mitigation strategy, J. Build. Eng. 65 (2023) 105756.
[67] M. Nedeljković, B. Ghiassi, G. Ye, Role of curing conditions and precursor on the microstructure and phase chemistry of alkali-activated fly ash and slag pastes, Materials 14 (8) (2021) 1918.
[68] W. Zhang, X. Yao, T. Yang, Z. Zhang, The degradation mechanisms of alkali-activated fly ash/slag blend cements exposed to sulphuric acid, Constr. Build. Mater. 186 (2018) 1177–1187.
[69] N. Marjanović, M. Komljenović, Z. Baščarević, V. Nikolić, Comparison of two alkali-activated systems: mechanically activated fly ash and fly ash-blast furnace slag blends, Procedia Eng. 108 (2015) 231–238.
[70] A. Rafeet, R. Vinai, M. Soutsos, W. Sha, Effects of slag substitution on physical and mechanical properties of fly ash-based alkali activated binders (AABs), Cem. Concr. Res. 122 (2019) 118–135.
[71] C. Li, H. Sun, L. Li, A review: The comparison between alkali-activated slag (Si+ Ca) and metakaolin (Si+ Al) cements, Cem. Concr. Res. 40 (9) (2010) 1341–1349.